2007. 2
Master's Thesis

A Study on the Analytical Model For Laser Key Hole

Graduate School of Chosun University

Department of Ocean Engineering and

Naval Architecture

C. Pramod

A Study on the Analytical Model For Laser Key Hole

February 2007

Graduate School of Chosun University

Department of Ocean Engineering and

Naval Architecture

C. Pramod

A Study on the Analytical Model For Laser Key Hole

Advisor : Professor Han-Sur Bang

A Thesis submitted for the degree of

Master of Engineering

October 2006

Graduate School of Chosun University

Department of Naval Architecture and

Ocean Engineering

C. Pramod

朴 鎬 慶의 碩士學位 論文을 認准함

委員長　朝鮮大學校 敎授　房 熙 善 ________

委　員　朝鮮大學校 敎授　房 漢 瑞 ________

委　員　朝鮮大學校 敎授　尹 德 榮 ________

2006 年　11 月

朝鮮大學校大學院

CONTENTS

ABSTRACT

A Study on the Mathematical Model for Laser Keyhole Using Existing Models and Experimental Verification by Nd-YAG Laser Keyhole Welding

C.Pramod
Advisor: Prof. Han-Sur Bang PhD
Department of Producing and Processing
Graduate School of Chosun University

Numerous models for the laser welding have improved the understanding of the laser welding. A model of deep penetration welding was developed by A Kaplan has been studied in detail and verified using experimentation. A heat transfer analysis and a residual stress analysis are performed to further verify the model.

List of Figures

List of Tables

Chapter 1

INTRODUCTION

1.1 Basic Introduction

Laser welding is becoming more and more popular in the welding field for a wide range of applications. This section discusses the laser welding process in brief. In the latter part of the section, the fundamentals of analytical modeling are discussed, which has become quite popular in the field of welding.

1.1.1 Laser Welding

Laser welding is a commercial process used extensively to weld a wide range of materials. The laser beam is focused toward a seam or area which causes the materials to from change from solid to liquid and, as the laser energy is removed, back to solid. Laser welding is a type of fusion welding which may be used to produce selective area spot welds or linear continuous seam welds. There are two types of laser welding processes, conduction and penetration. Laser conduction welding relies on the conductivity of the material being welded. The laser beam is focused on a specific area on the material which by proximity will conduct heat into the joint area to be welded. By focusing laser beam at a location, heat is generated which is conducted into the joint causing the material change from a solid to a liquid and combine to the two separate liquid materials. After the material from the two material changes back to a solid the two materials are joined or welded at that location. Laser conduction welds are used for spot welding, continuous and partial penetration seam welding. Laser penetration welding is produced by focusing the laser beam energy at a single location until the stacked materials are heated to a liquid state and some of the material vaporizes creating a hole within the material equal to the thickness of the material. When the stacked materials cool from a liquid to a solid state the material has been joined at that location through both stacked materials.

There are two common types of laser welding technologies in use,

- CO_2 Gas laser
- Solid state lasers (YAG type)

CO_2 lasers use a mixture of high purity carbon dioxide with helium and nitrogen as the lasing medium.

YAG lasers use a solid bar of yttrium aluminum garnet doped with neodymium as the lasing medium.

Both CO_2 and YAG lasers can operate in either continuous or pulsed operating modes.

1.1.2 Analytical Models

Analytical models are mathematical models that have a closed form solution, i.e. the solution to the equations used to describe changes in a system can be expressed as a mathematical analytic function.

Models provide an economical description of the essential features of a complex situation. The discipline of constructing models helps us to get our thinking straight; it makes us get down to fundamental principles; the process of modeling helps us to learn how to formulate problems better, (especially those broad, fuzzy problems where it is hard to know how and where to begin) and how to identify essential elements needed for moving toward explanation and for communicating with others. Formal analytical models enable us to use more variables than we can comfortably carry in our heads. By temporarily setting aside unimportant variables, they serve as powerful tools for the study of interrelationships among the important variables.

As we use models more and more, we begin to develop analytic insights in other situations where we do not consciously engage in a modeling process.

1.2 Scope and Objective

When a laser beam is brought to focus at or near the surface of a metal during laser welding, the majority of the incident energy is reflected back from the work piece. This is due to the fact that most metals are good reflectors of the 10.6mm wavelength light energy.

At an incident energy of above approximately 105 W/cm^2 the small amount of energy that is absorbed is sufficient to heat the metal surface and produce plasma above the work piece. Under favorable conditions and at an incident energy above 106 W/cm^2 the rapid removal of metal by vaporization leads to the formation of a small keyhole into the work piece.

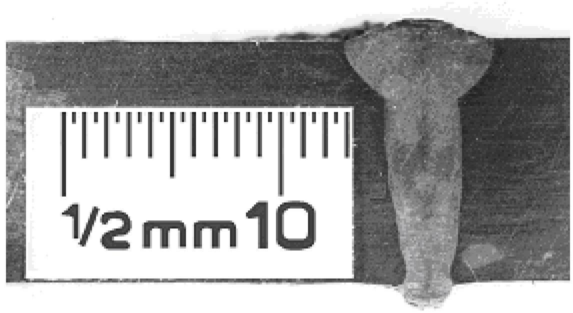

Figure 1. 1 Key Hole Shape

The effective coupling efficiency is further increased by the presence of the keyhole since multiple reflections of the laser take place on the keyhole walls and hence the keyhole is able to penetrate deeper into the work piece. The keyhole itself is held open by the vapor pressure, which prevents the walls from collapsing.

For Continuous Wave lasers, as the laser is moved along the joint line the molten metal flows round the keyhole and the molten walls at its trailing edge come together and solidify through the depth of the keyhole to form the weld.

There are significant advantages of this process over other welding processes, for example deep penetration and high welding speeds.

Due to the fact that heat is transferred not just to a point on the surface but to a line extending through the thickness of the material, the lateral heat spread is much smaller than conventional techniques, which removes a number of metallurgical problems such as mechanical deformation or chemical transformation.

Much higher weld speeds can be obtained than by conventional methods because of the keyhole effect, with the overall heat input still lower than conventional welding. The deep penetration allows several layers of material to be lap welded in a single pass. Dissimilar metals or metals of different thickness may be welded, which is not possible using any other welding technique.

A model of deep penetration laser welding was developed by A Kaplan based on calculation of the keyhole profile. The thermodynamics and the flow of metal vapour inside the keyhole have been calculated. The beam damping due to the plasma plume above the work piece and the mean plasma absorption coefficient in the keyhole is estimated. A detail study of this model is performed and the mathematical model is verified by experiment using Nd-YAG laser welding. Further a residual stress analysis and a heat transfer analysis is performed to confirm this.

1.3 Literature Review

This section describes the development processes in the field of laser welding and its future in the industry. The second part of the section gives an outline of the mathematical model development and the existing keyhole mathematical models and their features.

1.3.1 Future Developments in Laser Welding

The number of applications for laser beam welding in industry continues to grow. The specific advantages of laser welding in comparison to conventional welding techniques are the low energy per section (little distortion of components), the opportunities opened by deep penetration welding (overlap joints) and the broader spectrum of weldable materials.

Within the scope of public-funded research projects and research projects for industry extensive results about metal welding have been obtained.

For the automotive industry in particular, joining processes for numerous applications, such as car bodies and functional elements but also gear wheels, wheel rims, shift-forks and accumulators, have been developed. By means of an appropriate process management even steel with a high carbon content can be welded free of cracks. The forming characteristics can be guaranteed by means of a downstream or integrated local thermal treatment.

For welding applications with higher demands on the gap bridging ability, MIG hybrid welding is being qualified for sheet steel and magnesium. Filler material is molten by the arc and can be added without negative effects on the welding speed.

In the field of light metals many applications for aluminum have been implemented in industry. LZH carried out investigations on laser beam welding of aluminum cast and extrusion materials; the results were used for the development of aluminum car bodies. Even difficult-to-weld alloys can be welded by modern high-power lasers. Metallurgical restraints, such as the high hot brittleness of certain alloys, can be overcome by means of a customized process technique and the controlled use of filler material.

Future-oriented investigations are currently focused on magnesium and titanium alloys. The use of these light metals is of great importance to both the transportation and medical technology.

Besides welding and metallurgy-relevant developments, LZH develops process-technical solutions consisting of customized system technology, processing heads and clamping tools.

Laser brazing can be used for various metals that are not weldable due to their composition or for joining processes where the thermal exposure of the parts should be reduced. In many cases, a bonded joint of metals that are not of the same kind can only be generated using laser brazing.

In addition, laser brazed seams fulfill high optical demands on the seams. Besides the joining of ceramics and metals, laser brazing of carbide metal cutting edges of buzz saw blades or the manufacturing of tailored hybrid blanks made of steel and aluminum using laser brazing were investigated within the scope of public-funded projects, too.

Numerous laser brazing processes for components for the automobile technology, motive power engineering, medical technology and electronics were qualified in line with industry projects.

1.3.2 Existing Analytical Models for Laser welding

Numerous models of laser welding have improved the physical understanding of the process. A brief review has been given by Kapadia (Schu6cker 1993).

The stationary temperature field in the work piece was calculated analytically by introducing a moving line source of heat (Rosenthal 1946). By superimposition of a point source the typical bottle-shaped weld seam cross section can be mathematically described (Steen eta1 1988).

To keep the keyhole open, the energy balance and the pressure balance at the keyhole wall must be satisfied (Andrews and Atthey 1976). The metal vapor inside the keyhole acts against the surface tension to keep the keyhole open (Klemens 1976). The metal vapor flows out of the keyhole (Andrews and Atthey 1976, Dowden et a1 1987) and is continuously replaced by evaporated material. Nevertheless, only few percent of the molten material are evaporated (Klemens 1976), but the major part of the melt is accelerated due to pressure gradients and passes sideward around the keyhole (Beck et al 1991).

The power is directly absorbed at the surface by Fresnel absorption, but also plasma absorption occurs (Dowden et a1 1987). The metal vapour reaches temperatures much higher than the evaporation temperature, resulting in strong ionization. The resulting plasma absorbs the infrared radiation of a CO_2 laser mainly by the effect of inverse Bremsstrahlung. Another absorption mechanism is Fresnel absorption due to multiple reflections of the beam inside the keyhole (Beck et al 1992, Kar et a1 1992).

Whereas existing practicable models (Swift-Hook and Gick 1973, Schuijcker 1992) are based on major simplifications for such features as the keyhole geometry, more sophisticated models calculate the keyhole profile point-by-point with more computational effort. This has been done for rotational keyhole symmetry by several authors (Andrews and Atthey 1976, Dowden et a1 1987, Wei et a1 1990, Beck et a1 1992, Kar et al 1992).

The assumption of rotational symmetry restricts these models to low welding speeds. The model described in this work is an attempt to extend the calculation of the keyhole profile to higher welding speeds (Kaplan 1992, 1994).

The below table shows the step by step development of the numerical models for the laser key hole.

Table 1.1 Development of numerical models

Author	Type of work
Rosenthal, 1946	Analytical calculation of stationary temperature field in work piece
Andrews & Atthey, 1976	Energy Balance and Pressure Balance to keep keyhole open
Klemens, 1976	Metal vapour and surface tension to keep keyhole open
Dowden et al, 1987	Metal vapour flow and replacement by evaporated material, Fresnal and Plasma Absorption.
Steen et al, 1988	Mathematical representation of typical bottle shaped weld seam cross section
Beck et al, 1991	Melt acceleration due to pressure gradients & Multiple reflections

Chapter 2

NUMERICAL SIMULATION OF LASER KEY HOLE

2.1 Introduction

During the welding, the weldment is subjected to complex thermal cycles by welding heat source which results in the residual stresses, metallurgical change and distortion. In order to reduce these problems, it is necessary to predict the temperature distribution that develops in the weldment. This chapter discusses the heat transfer analysis and residual stress calculation basics. In the latter part, the use of Finite Element Analysis to predict the external flow rate and residual stress is also discussed in brief.

2.2 Heat Distribution and Numerical Simulation.

In the simplest of terms, the discipline of heat transfer is concerned with only two things: temperature, and the flow of heat. Temperature represents the amount of thermal energy available, whereas heat flow represents the movement of thermal energy from place to place.

On a microscopic scale, thermal energy is related to the kinetic energy of molecules. The greater a material's temperature, the greater the thermal agitation of its constituent molecules (manifested both in linear motion and vibrational modes). It is natural for regions containing greater molecular kinetic energy to pass this energy to regions with less kinetic energy.

Several material properties serve to modulate the heat transferred between two regions at differing temperatures. Examples include thermal conductivities, specific heats, material densities, fluid velocities, fluid viscosities, surface emissivities, and more. Taken together, these properties serve to make the solution of many heat transfer problems an involved process.

2.2.1 Theory and FEM formulation

The spatial and temporal temperature distribution satisfies the following governing equation of un-stationary heat conduction :

$$\rho c \frac{\partial T}{\partial t} = \lambda \nabla^2 T + \dot{Q} \tag{2.1}$$

where T is temperature (℃), ρ is density (g/㎤), $\dot{Q}$ is rate of temperature change due to heat generation per volume (cal/㎤・sec), t is time (sec), λ is thermal conductivity of isotropic material (cal/cm・sec・℃) and c is specific heat (cal/g・℃).

To solve this equation of un-stationary heat conduction, following boundary conditions are applied according to the kinds of problem.

• When the temperature is determined on the boundary S_1 :

$$T = \overline{T} \tag{2.2}$$

where $\overline{T}$ is determined temperature.

• When the heat flux, q_0 , flows from the boundary S_2 :

$$q = q_0 \tag{2.3}$$

• When heat transfer is on the boundary S_3 for convection:

$$q = \alpha_c (T - T_c) \tag{2.4}$$

where α_c is heat transfer coefficient for convection (cal/cm^2・sec・℃), T is boundary temperature of the object (℃), and T_c is the outside temperature of the object (℃).

• When heat radiation is on the boundary S_4:

$$q = \sigma F(T^4 - T_r^{\ 4}) \tag{2.5}$$

where σ is the Stefan Boltzmann constant, F is a compensation coefficient of shape, and T_r is the temperature of radiation source (℃). This equation can be transformed to the form of linear equation for the ease of processing as follows:

$$q = \alpha_r (T - T_r) \tag{2.6}$$

where

$$\alpha_r = \sigma F(T + T_r)(T^2 + T_r^{\ 2}) \tag{2.7}$$

Heat flux, q (cal/cm^3 · sec · ℃), in normal direction on the boundary is derived from the Fourier law as below:

$$q = -\lambda \frac{\partial T}{\partial n} \tag{2.8}$$

Heat conduction problem for the object of analysis is formulated as the finite element method using Galerkin method. Internal temperature of the element, T, is given by

$$T(x, y, z, t) = [N(x, y, z)]\{\phi(t)\} \tag{2.9}$$

where $[N]$ is a shape function matrix shown the relation between nodal temperature and internal temperature of the element. $\{\phi\}$ is the vector of the nodal temperature of the element at time t.

If Galerkin method is applied in equation (2.1) using $[N]$ as a weighting function at this time, following equation is obtained.

$$\int_{V^e}[N]^T\left\{\lambda\left(\frac{\partial^2 T}{\partial x^2}+\frac{\partial^2 T}{\partial y^2}+\frac{\partial^2 T}{\partial z^2}\right)+\dot{Q}-\rho c\frac{\partial T}{\partial t}\right\}dV=0 \tag{2.10}$$

where superscript, T, shows transformation of matrix and subscript, V^e, shows the domain of element. The term of second order in partial differential equation (2.10) is changed using Green-Gauss theorem, a formula of partial integration, to the following equation.

$$\begin{aligned}&\int_{V^e}\lambda[N]^T\left(\frac{\partial^2 T}{\partial x^2}+\frac{\partial^2 T}{\partial y^2}+\frac{\partial^2 T}{\partial z^2}\right)dV=\\&-\int_{V^e}\lambda\left(\frac{\partial[N]^T}{\partial x}\frac{\partial T}{\partial x}+\frac{\partial[N]^T}{\partial y}\frac{\partial T}{\partial y}+\frac{\partial[N]^T}{\partial z}\frac{\partial T}{\partial z}\right)dV+\int_{S^e}\lambda[N]^T\left(\frac{\partial T}{\partial n}\right)dS\end{aligned} \tag{2.11}$$

where S^e is the boundary of element.

If equation (2.9) and equation (2.2), Fourier's law, are substituted in equation (2.11), the right side of equation (2.11) becomes as bellows:

$$\begin{aligned}&-\int_{V^e}\lambda\left(\frac{\partial[N]^T}{\partial x}\frac{\partial[N]}{\partial x}+\frac{\partial[N]^T}{\partial y}\frac{\partial[N]}{\partial y}+\frac{\partial[N]^T}{\partial z}\frac{\partial[N]}{\partial z}\right)dV\cdot\{\phi(t)\}\\&-\int_{S^e}q[N]^T\,dS\end{aligned} \tag{2.12}$$

Using equation (2.12), equation (2.10) becomes finally as follows:

$$\begin{aligned}&-\int_{V^e}\lambda\left(\frac{\partial[N]^T}{\partial x}\frac{\partial[N]}{\partial x}+\frac{\partial[N]^T}{\partial y}\frac{\partial[N]}{\partial y}+\frac{\partial[N]^T}{\partial z}\frac{\partial[N]}{\partial z}\right)dV\cdot\{\phi(t)\}\\&-\int_{S^e}q[N]^T\,dS+\int_{V^e}\dot{Q}[N]^T\,dV-\int_{V^e}\rho c[N]^T[N]dV\cdot\frac{\partial\{\phi(t)\}}{\partial t}=0\end{aligned} \tag{2.13}$$

Simplifying above equation (2.13), un-stationary heat conduction problem can be expressed as following finite element expression for an element.

$$[k]\{\phi\}+[c]\left\{\frac{\partial\phi}{\partial t}\right\}=\{f\} \qquad (2.14)$$

where $[k]$, $[c]$ and $\{f\}$ show the heat conductivity matrix of an element, the heat capacity matrix of an element and the heat flow vector of an element, respectively. They are expressed as follows:

$$[k]=\int_{V^e}\lambda\left(\frac{\partial[N]^T}{\partial x}\frac{\partial[N]}{\partial x}+\frac{\partial[N]^T}{\partial y}\frac{\partial[N]}{\partial y}+\frac{\partial[N]^T}{\partial z}\frac{\partial[N]}{\partial z}\right)dV \qquad (2.15)$$

$$[c]=\int_{V^e}\rho c[N]^T[N]dV \qquad (2.16)$$

$$\{f\}=\int_{V^e}\dot{Q}[N]^T dV-\int_{S^e}q[N]^T dS \qquad (2.17)$$

Boundary conditions on the boundary S_2 to S_4 can be given to substitute q in second term of equation (2.17) using equation (2.3), (2.4) and (2.6).

• When the heat flux, q_0, flows from the boundary S_2:

From the equation (2.3), $$\int_{S_2^e}q[N]^T dS=\int_{S_2^e}q_0[N]^T dS \qquad (2.18)$$

In the case of adiabatic boundary condition, q_0 become zero (0).

• When heat transfer is on the boundary S_3 for convection:

From the equation (2.4), $$\int_{S_3^e}q[N]^T dS=\int_{S_3^e}\alpha_c(T-T_c)[N]^T dS \qquad (2.19)$$

If T in the equation (2.19) is substituted by the equation (2.9), the equation (2.19) become as bellows:

$$\int_{S_3^e} q[N]^T dS = \int_{S_3^e} \alpha_c [N]^T [N] dS \cdot \{\phi(t)\} - \int_{S_3^e} \alpha_c T_c [N]^T dS \qquad (2.20)$$

• When heat radiation is on the boundary S_4:

From the equation (2.6), $$\int_{S_4^e} q[N]^T dS = \int_{S_4^e} \alpha_r (T - T_r)[N]^T dS \qquad (2.21)$$

If T in the equation (2.21) is substituted by the equation (2.9), The equation (2.21) becomes as bellows:

$$\int_{S_4^e} q[N]^T dS = \int_{S_4^e} \alpha_r [N]^T [N] dS \cdot \{\phi(t)\} - \int_{S_4^e} \alpha_r T_t [N]^T dS \qquad (2.22)$$

From the above conditions, general boundary condition eliminated first boundary condition when the temperature is determined on the boundary S_1 can be applied to solve the un-stationary heat conduction problem.

Equation (2.15) and (2.17) are modified using equation (2.18), (2.20) and (2.22) as follows:

$$\begin{aligned}[k] = &\int_{V^e} \lambda \left(\frac{\partial [N]^T}{\partial x} \frac{\partial [N]}{\partial x} + \frac{\partial [N]^T}{\partial y} \frac{\partial [N]}{\partial y} + \frac{\partial [N]^T}{\partial z} \frac{\partial [N]}{\partial z} \right) dV \\ &+ \int_{S_3^e} \alpha_c [N]^T [N] dS + \int_{S_4^e} \alpha_r [N]^T [N] dS \end{aligned} \qquad (2.23)$$

$$\{f\} = \int_{V^e} \dot{Q} [N]^T dV - \int_{S_2^e} q_0 [N]^T dS + \int_{S_3^e} \alpha_c T_c [N]^T dS + \int_{S_4^e} \alpha_r T_r [N]^T dS \qquad (2.24)$$

Therefore, finite element formula of an element can be derived as a form of matrix equation including boundary conditions by using equation (2.16), (2.23) and (2.24).

Finite element formula for the whole object analyzed is constructed with assembled each matrix of elements and it can be expressed as follows:

$$[K]\{\Phi\}+[C]\left\{\frac{\partial \Phi}{\partial t}\right\}=\{F\} \tag{2.25}$$

where $[\Phi]$, $[K]$, $[C]$ and $\{F\}$ show the vector of the nodal temperature in the whole object, the heat conductivity matrix in the whole object, the heat capacity matrix in the whole object and the heat flow vector in the whole object, respectively. They are given as bellows.

$$[\Phi]=\sum_e \phi,\ [K]=\sum_e k,\ [C]=\sum_e c,\ \{F\}=\sum_e f \tag{2.26}$$

2.2.2 Finite Element Coding Flow chart

Using this formulation the finite element code is developed for the heat transfer analysis. The developed code consist of 28 subroutines and according to the task performed, subroutines can be grouped accordingly as shown in the block diagram of Fig. 2. 1

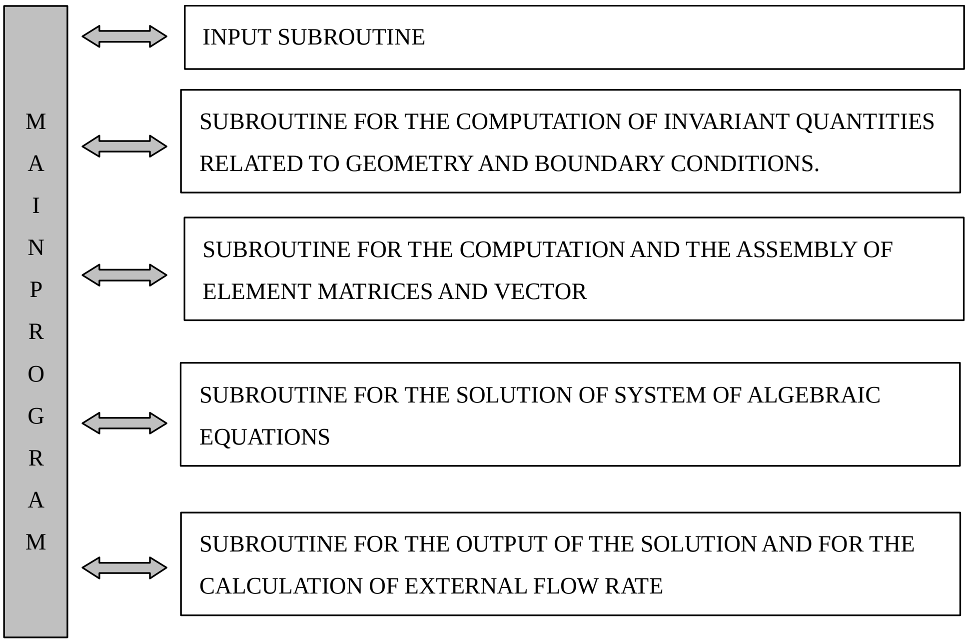

Figure 2. 1 Structure of Heat Transfer analysis program

2.3 Residual Stresses and Numerical Simulation.

Deterioration of material and welding residual stresses caused during welding reduce the stability in the welded. These effects are quite different according to the welding methods (i.e. according to the various heat sources). Therefore, it is necessary to predict the mechanical behaviors and properties of welds accurately before welding. The deterioration of material and welding residual stresses are caused by spatial and temporal temperature distribution in regions a short distance from heat source. In order to predict accurately these properties, therefore, the thermal elasto-plastic analysis is required to examine their history. A finite element method has been applied actively to perform this analysis.

2.3.1 Basic considerations of Elasto-Plastic Analysis

For welding residual strength analysis, the solid is assumed to be isotropic and the mechanical properties of the material such as yield stress, Young's modulus, thermal expansion coefficient etc are dependent on the temperature changes in both elastic and plastic region. In the plastic region, Plastic-flow theory is adapted, besides, Von-Mises condition is used as the yield function considering linear equivalent hardening law. All the basic equations used are given in the matrix form as follows.

2.3.1.1 Equilibrium equation

The equilibrium equation can be replaced by the principle of virtual work.

$$\int_V \delta\{\varepsilon\}^T \{\sigma\} dV - \int_V \delta\{U\}^T \{\overline{F}\} dV - \int \delta\{U\}^T \{\overline{T}\} dS = 0 \qquad (2.27)$$

where $\{\sigma\}$:stress vector, $\{\varepsilon\}$:strain vector, $\{U\}$:displacement vector, $\{\overline{F}\}$:body force vector per unit volume, $\{\overline{T}\}$:surface force vector per unit area, V : volume of an object, and S_σ : area given mechanical boundary condition.

2.3.1.2 Equation of strain-displacement relation

$$\{\varepsilon\} = [A]\{U\} \quad (2.28)$$

where matrix $[A]$ includes the differential operator.

2.3.1.3 Equation of stress-strain relation

$$\{\varepsilon\} = \{\varepsilon^e\} + \{\varepsilon^T\} \quad (2.29)$$

where $\{\varepsilon\}$: total strain vector, $\{\varepsilon^e\}$:elastic strain vector and $\{\varepsilon^T\}$: thermal strain vector. The relation between $\{\sigma\}$ and $\{\varepsilon^e\}$ follows the Hook's law and is expresses as bellows.

$$\{\sigma\} = [D^e]\{\varepsilon^e\} \quad (2.30)$$

where $[D^e]$ is elastic stress-strain matrix. From the equation (2.29) and (2.30), an equation of stress-strain relation is obtained as follows.

$$\{\sigma\} = [D^e](\{\varepsilon^e\} - \{\varepsilon^T\}) \quad (2.31)$$

Divide an object in finite element, a displacement vector of inside finite element $\{U\}$ can be expressed using an unknown displacement vector in nodal point $\{d\}$ as bellows.

$$\{U\} = [N]\{d\} \quad (2.32)$$

where $[N]$ is a shape function matrix. If $\{U\}$ in the equation (2.28) is substituted by the equation (2.32)

$$\{\varepsilon\} = [A][N]\{d\} = [B]\{d\} \quad (2.33)$$

where $[B]$ is a strain-displacement matrix. Using equation from (2.31) to (2.33), equation for principle of virtual work (2.27) is modified as bellows.

$$\int_{V^e} \delta\{d\}^T [B]^T [D^e](\{B\}\{d\} - \{e^T\})dV - \int_{V^e} \delta\{d\}^T [N]^T \{\overline{F}\}dV - \int_{S_\sigma^e} \delta\{d\}^T [N]^T \{\overline{T}\}dS = 0 \quad (2.34)$$

where V^e and S_σ^e show the volume of element and the element area given mechanical boundary condition, respectively. Equation (2.34) is rearranged as following form.

$$\delta\{d\}^T \int_{V^e} [B]^T \left[D^e\right][B] dV \{d\}$$
$$= \delta\{d\}^T \int_{S_\sigma^e} [N]^T \{\overline{T}\} dS + \delta\{d\}^T \int_{V^e} [N]^T \{\overline{F}\} dV + \delta\{d\}^T \int_{V^e} [B]^T \left[D^e\right]\{\varepsilon^T\} dV \tag{2.34}$$

For the constitution of above equation (2.34), following equation is to be constituted because $\delta\{d\}$ is a virtual displacement vector has some value in nodal point.

$$\int_{V^e} [B]^T \left[D^e\right][B] dV \{d\} = \int_{S_\sigma^e} [N]^T \{\overline{T}\} dS + \int_{V^e} [N]^T \{\overline{F}\} dV + \int_{V^e} [B]^T \left[D^e\right]\{\varepsilon^T\} dV \tag{2.35}$$

Therefore, equilibrium equation of element can be expressed as follows.

$$[k]\{d\} = \{f_s\} + \{f_v\} + \{f_T\} \tag{2.36}$$

where $[k]$: stiffness matrix of element, $\{f_s\}$: nodal force vector due to surface force, $\{f_v\}$: nodal force vector due to body force and $\{f_T\}$: pseudo nodal force vector due to thermal strain. These are consisted as bellows.

$$[k] = \int_{V^e} [B]^T \left[D^e\right][B] dV \{d\} \tag{2.37}$$

$$\{f_s\} = \int_{S_\sigma^e} [N]^T \{\overline{T}\} dS \tag{2.38}$$

$$\{f_v\} = \int_{V^e} [N]^T \left[\overline{F}\right] dV \tag{2.39}$$

$$\{f_T\} = \int_{V^e} [B]^T \left[D^e\right]\{\varepsilon^T\} dV \tag{2.40}$$

Equilibrium equation for the whole object, the total element, is obtained to assemble the equation (2.36) for each element.

2.3.2 Finite Element Coding Flow chart

The developed code consist of 47 subroutines and according to the task performed, subroutines can be grouped accordingly as shown in the block diagram of Fig. 2. 2

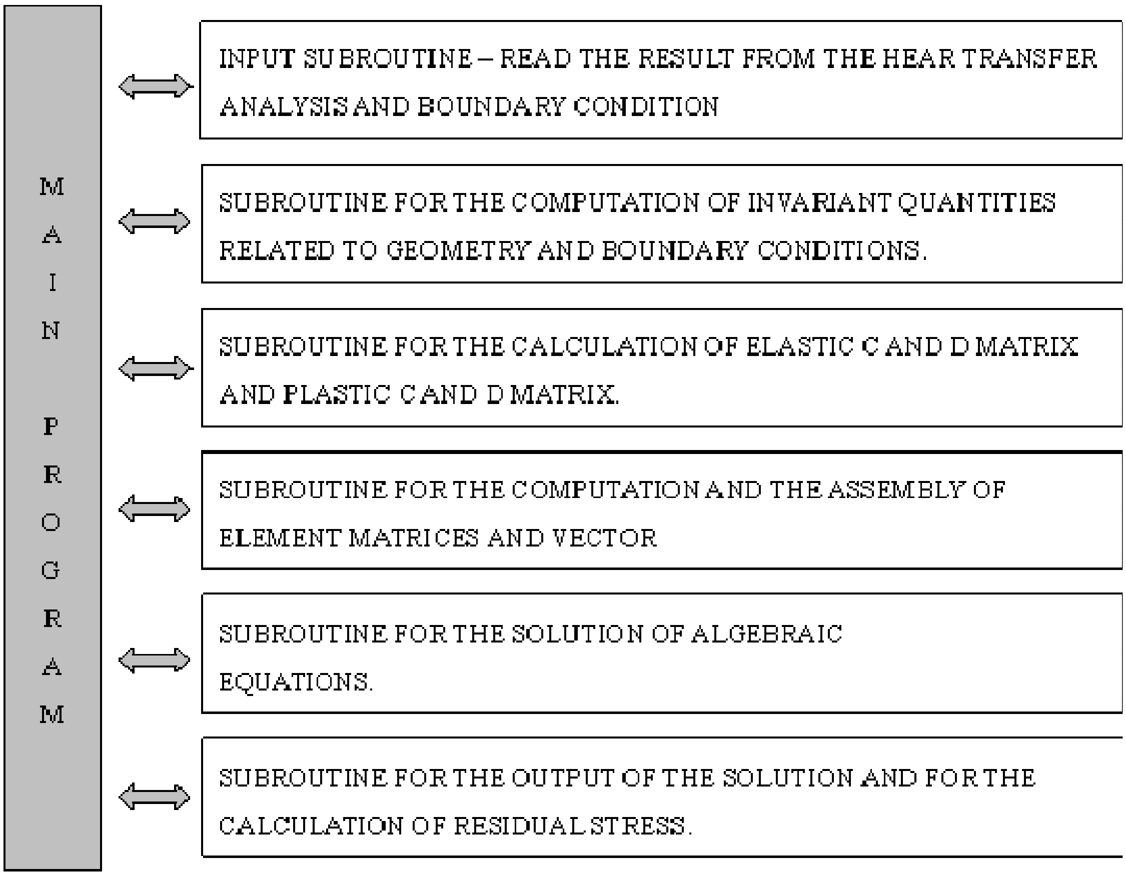

Figure 2. 2 Structure of Residual Stress analysis program

Chapter 3

ANALYTICAL MODEL OF LASER KEYHOLE PROFILE

3.1 Brief Outline

A. F. H. Kaplan, Professor is currently the Chair of Manufacturing/Laser Materials Processing, Luleå TU. He had developed a model of deep penetration laser welding based on calculation of the key hole profile. This chapter discusses in detail the mathematical model including the formulation. In the later part of this chapter various absorption mechanisms considered by Kaplan is described briefly. At the end of the chapter, his findings and conclusions are discussed in brief.

3.2 Mathematical Model formulation & Keyhole Calculations.

In this section, a brief description of the model is given. In the second part of this section, the formulation of the mathematical model is described in detail. The last part of this section describes the method to calculate the keyhole profile.

3.2.1 Model Description

This model describes the process of deep penetration laser welding by calculating the keyhole profile. A point by point determination of the energy balance at the keyhole wall is used to calculate the keyhole profile.

At first, a formula for the heat conduction is derived from the model of a moving line source of heat. The various absorption mechanisms are considered and modeled. The corresponding absorbed power transferred to the keyhole balances the conduction losses, which yields the local inclination of the wall. A detail derivation and explanation is given in the next section.

Further to the above, Kaplan has also calculated the beam damping due to the plasma plume above the work piece and the mean plasma absorption coefficient in the keyhole is estimated. The keyhole profile tends to a geometry that distributes the major part of the beam to the front wall owing to higher conduction losses in the upstream side. As the welding speed is increased, the energy abortion is decreased which are further discussed.

Even though many models existed prior to the model by Kaplan, they were either based on major simplifications for the keyhole geometry or needed more computational efforts.

Many existing practicable models based on keyhole rotational symmetry exist. The assumption of rotational symmetry restricts these models to low welding speed. The model by Kaplan is an attempt to extend the calculation of keyhole profile to higher welding speeds. Thus the keyhole wall is calculated both at the front wall and the back wall and the differing heat conduction results in an asymmetric profile. The energy balance necessary to obtain such a shape is described in the following section. From the keyhole profile the thermodynamic and gas dynamic vapour state in side the keyhole is calculated.

3.2.2 Model Formulations

The model formulation is further divided into two sections the heat losses at the keyhole wall and the absorbed beam power at the keyhole wall. Comparing both of the energy will result in the local inclination of the keyhole wall as described in the last section.

3.2.2.1 Heat losses at the Keyhole Wall.

In the following the coordinate system is alternatively Cartesian (x, y, z) with x being the coordinate in the welding direction, z the coordinate in the beam direction and y perpendicular to both, or in cylindrical coordinates (r, φ, z) with r and φ being the equivalent polar coordinates corresponding to x and y.

The geometry of the keyhole wall in the x-z plane may be calculated point-by-point by locally solving the energy balance at the wall, figure 3.l.

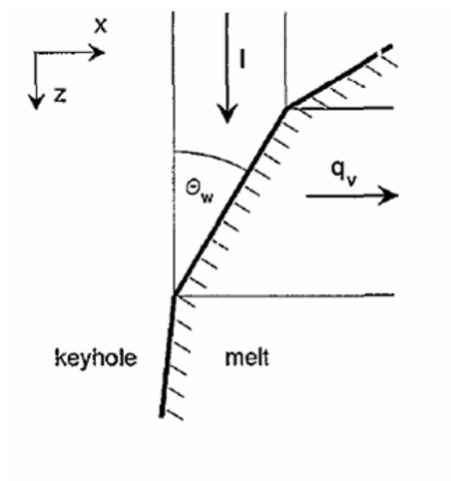

Figure 3. 1Energy Balance at the Keyhole

The energy balance compares the absorbed laser power to the power losses due to heat conduction and convection in the work piece. A formula for the heat flow from the keyhole wall into the work piece can be derived from the moving line source model (Rosenthal 1946). The latter gives a solution for the temperature field T(r, φ) in the work piece.

$$T(r,\varphi) = T_a + \frac{P'}{2\pi\lambda_{th}} K_0(P_e^{'} r) e^{-P_e^{'} r Cos\varphi} \tag{3.1}$$

With a modified Peclet number

$$P_e^{'} = {}^{v_\omega}\!/_{2\kappa} \tag{3.2}$$

T_a is the ambient temperature, λ_{th} denotes the thermal conductivity, & v_w is the welding speed and k is the thermal diffusivity. K_O ( ) is the modified Bessel function of second kind and zeroth order. The temperature field has a singularity at the origin, where the line source with power per unit depth P' is located.

From the temperature field (3.1) the heat flow inside the material may be derived. Equation (3.1) can be rearranged to calculate explicitly the source strength, P', which is necessary to reach evaporation temperature at an arbitrary point r, φ, which refers to a point on the keyhole wall:

$$P'(r,\varphi) = (T_v - T_a) 2\pi\lambda_{th} \frac{1}{K_0(P_e^{'} r)} e^{P_e^{'} r Cos\varphi} \tag{3.3}$$

The heat flow q may be determined by Fourier's law of heat conduction that can be simplified by considering only the radial component

$$q = -\lambda_{th}\nabla T \approx -\lambda_{th}\frac{\partial T}{\partial r} \tag{3.4}$$

Spatial derivation of the temperature of the Rosenthal solution (3.1) with respect to r leads to

$$\frac{\partial T}{\partial r} = \frac{P'(r,\varphi)}{2\pi\lambda_{th}} P_e^{'}[-K_0(P_e^{'}r)Cos\varphi + K_0^{'}(P_e^{r})]e^{-P_e^{'}rCos\varphi} \tag{3.5}$$

For the derivation K0' ( ) of the Bessel function the following relation is valid (Bronstein and Semendjajew 1985):

$$K_o^{'}(x) = -K_1(x) \tag{3.6}$$

where K_1 ( ) is the modified Bessel function of second kind and first order. By inserting (3.5) and (3.6) the heat flow equation (3.4) becomes:

$$q(r,\varphi) = -\lambda_{th}\frac{\partial T}{\partial r} = \frac{P'(r,\varphi)}{2\pi} P_e^{'}[K_0(P_e^{'}r)Cos\varphi + K_1(P_e^{r})]e^{-P_e^{'}rCos\varphi} \tag{3.7}$$

If we consider the boundary condition that the evaporation temperature T_V, shall be reached at the keyhole wall, then equation (3.3) can be applied for the source strength P' in (3.7) and the heat flow q_V, for an arbitrary point r, φ at the evaporation temperature is

$$q_v(r,\varphi) = (T_v - T_a)\lambda_{th}P_e^{'}\left(Cos\varphi + \frac{K_1(P_e^{'}r)}{K_0(P_e^{'}r)}\right) \tag{3.8}$$

Equation (3.8) is the main formula for the model used to describe the heat losses at each point of the keyhole wall.

To obtain the keyhole profile in the x-z plane, only the azimuthal angles φ = 0, π are of interest, describing the heat losses of any point x_f at the front wall (φ = 0)

$$q_v(x_f) = (T_v - T_a)\lambda_{th}P_e^{'}\left(1 + \frac{K_1(P_e^{'}r)}{K_0(P_e^{'}r)}\right) \tag{3.9}$$

and of any point x_r at the rear wall (φ = π).

$$q_v(x_r) = (T_v - T_a)\lambda_{th}P_e^{'}\left(-1 + \frac{K_1(P_e^{'}r)}{K_0(P_e^{'}r)}\right) \tag{3.10}$$

3.2.2.2 Absorbed Beam Power at the Keyhole Wall.

In the simplest case, the locally absorbed beam power at the keyhole wall can be described by considering only the Fresnel absorption of the beam intensity distribution I(r, φ, z) hitting the surface.

The intensity of the laser beam has in its simplest case a Gaussian-like distribution (Hugel 1992) as follows.

$$I(r,\varphi,z) = I(x,z) = I_0\left(\frac{r_f}{r_{f0}}\right)^2 \exp\left(-\frac{2r^2}{r_f^2}\right) \tag{3.11}$$

where I_0 is the peak intensity, r_f is the beam radius, r_{f0} is the focal radius.

The focal radius r_{f0} can be determined from the focusing number F of the focusing optics, the wavelength λ and beam quality M^2.

$$r_{fo} = \frac{2\lambda F M^2}{\pi} \tag{3.12}$$

In order to calculate the variation of beam radius over the depth we define the Rayleigh length, z_r as follows.

$$z_r = \pm 2 r_{f0} F \tag{3.13}$$

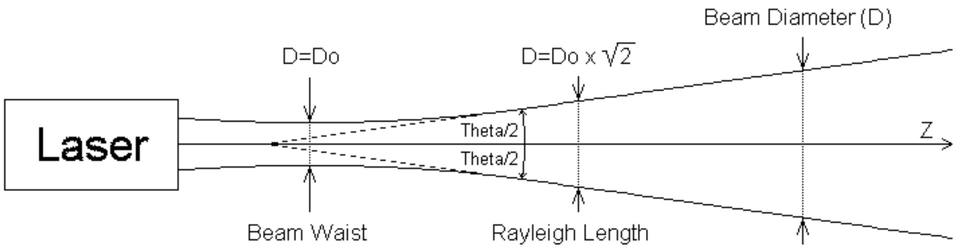

Figure 3. 2 Laser Beam radius variation along the depth

Once the Rayleigh length is calculated, the beam radius $r_f(z)$ varying over the depth is given by the following expression.

$$r_f(z) = r_{f0}\left[1+\left(\frac{z-z_0}{z_r}\right)^2\right]^{1/2} \tag{3.14}$$

where z_0 is the position of the focal plane relative to the upper surface of the work piece. The work positive values are in the beam direction.

The peak intensity I_0, depends on the laser power, P_L and the focal radius, r_{f0} as given in the following relation.

$$I_0 = \frac{2P_L}{r_{f0}^2 \pi} \tag{3.15}$$

Substituting (3.12), (3.14) and (3.15) in (3.11) we get,

$$I(r,\varphi,z) = I(x,z) = \frac{2P_L}{r_{f0}^2 \pi}\left(1+\left(\frac{z-z_0}{z_r}\right)^2\right)\exp\left(-\frac{2r^2}{r_{f0}^2\left[1+\left(\frac{z-z_0}{z_r}\right)^2\right]}\right) \tag{3.16}$$

3.2.2.3 Energy Balance at the Keyhole Wall.

The energy balance compares the heat losses (3.8) to the absorbed intensity I_a, which is the incident laser intensity multiplied by an absorption coefficient. The inclination angle of the keyhole wall accounts for the difference by making a geometrical transformation to fulfill the energy balance, see figure 3.1.

The energy balance is solved in a consecutive manner in the x-z plane starting far away from the beam ($x >> r_f$, $z = 0$) and integrating radially inwards, as can be seen in figure 3.3 in the next page.

According to the figure 3.1, the local energy balance at the key hole wall is;

$$Tan(\theta_w) = \frac{q_v(x)}{I_a(x,z)} = f(x,z) \tag{3.17}$$

which yields the local wall angle θ_w.

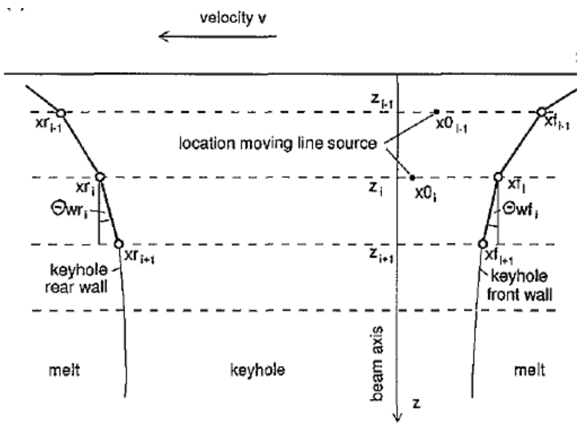

Figure 3. 3 Key Hole Profile

Considering the absorbed power is equal to the laser intensity absorbed by Fresnel absorption, $I_{a,Fr}$ equation (3.17) can be modified as follows.

$$Tan(\theta_w) = \frac{q_v}{\alpha_{Fr}(\theta)I} = \frac{q_v}{I_{a,Fr}} \tag{3.18}$$

The further absorption mechanisms of plasma absorption due to inverse Bremsstrahlung $I_{a,iB}$ and Fresnel absorption during multiple reflections $I_{a,mr}$ are considered in the following way.

$$Tan(\theta_w) = \frac{q_v - I_{a,iB} - I_{a,mr}}{I_{a,Fr}(\theta_w)} \tag{3.19}$$

The direct geometrical relation to the wall angle is only influenced by direct Fresnel absorption whereas the other absorption mechanisms can be simplified to act in the horizontal plane of the heat flow and are therefore subtracted from it. The various absorption mechanisms are dealt with in the later section.

3.2.3 Calculation Procedure

The calculation procedure for the keyhole profile is shown in the figure 3.3 above. By considering discrete values of z_i, the keyhole wall angle is calculated from the top surface downwards point by point simultaneously for the front and back walls. Each angle leads to the value of the next element. The location of the moving line source is different for each element and not equal to the beam axis but can be defined by the distance between the points x_f and x_r.

For each distance there exists only one line source P’, which then determines its location x_0 and the heat flow from equation (3.8). Then the wall angle results from the energy balance (3.17) and the wall points x_f and x_r of the following element can be calculated.. The full keyhole profile is obtained when the front wall and the back wall point crosses.

3.3 Absorption Mechanisms

The incident laser intensity is altered by several absorption effects that are included in the model according to the flow diagram, figure 3.4. In other words, the values used in the equation (3.19) results from the following absorption sequence.

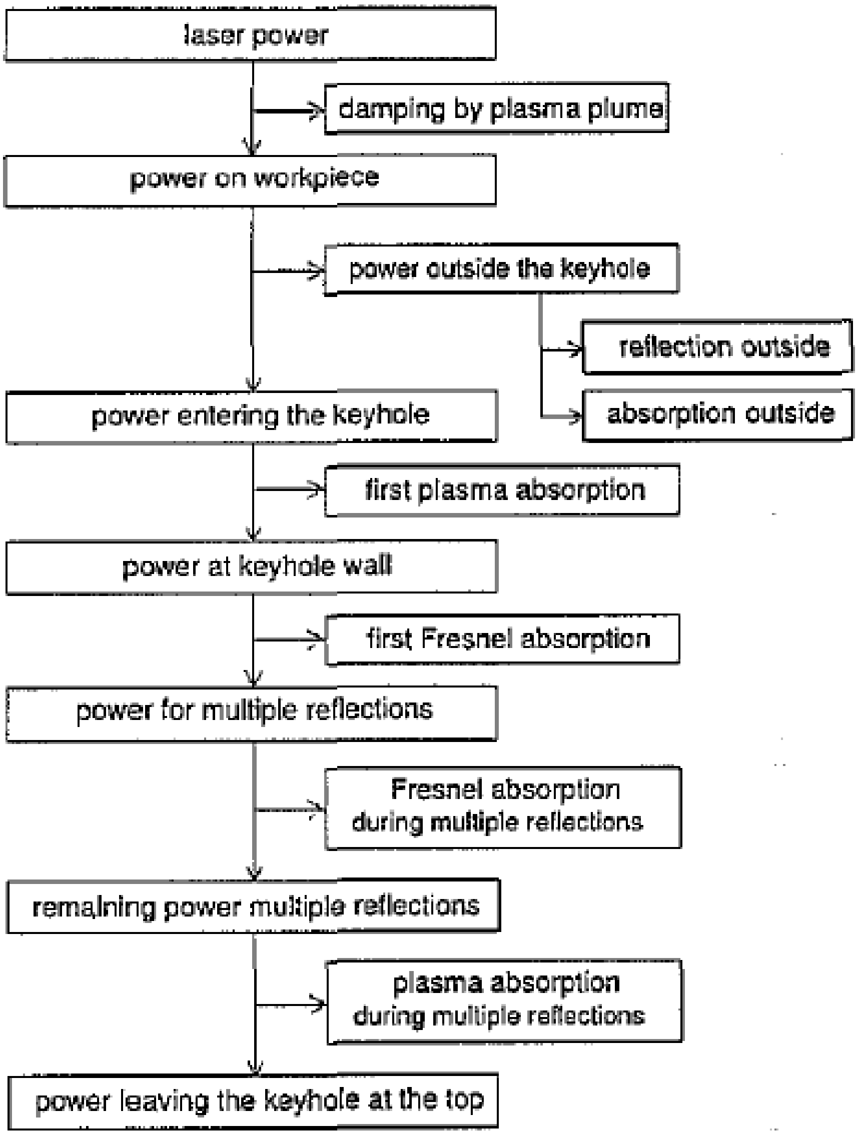

Figure 3. 4 Flow Diagram of Absorption Mechanism

3.3.1 Damping by plasma plume

The damping of the incident power due to a plasma plume above the keyhole can be estimated, if the mean height h_{pl} of the metal vapour plume over the work piece is known. The absorbed fraction of the beam is

$$\alpha_{pl} = 1 - \exp(-\alpha_{ib} h_{pl}) \tag{3.20}$$

where h_{pl} is the plume height and α_{ib} is the Bremsstrahlung coefficient which is temperature dependent. A mean value of $\alpha_{ib} = 100\ m^{-1}$ can be used.

3.3.2 Power outside the keyhole wall.

The power hitting the work piece outside the keyhole is strongly reflected and only a small part is absorbed because the normal incidence leads to low Fresnel absorption. The effect is implicitly included in the model due to the fact that the angle resulting from the energy balance will be nearly horizontal if the absorbed intensity is sufficiently low. For this case no further absorption effects due to multiple reflections and plasma absorption will be considered for these wall points. A critical angle of $\pi/2$ is defined, which indicates the starting point of the keyhole, where the other absorption effects also occur.

3.3.3 First plasma absorption.

The plasma absorption before hitting the keyhole wall for the first time is included by assuming the mean path of the partial beams to be equal to the half depth of the keyhole, as calculated in the first run. A mean value, $\alpha_{ib,1}$ for this plasma absorption coefficient is used.

$$\alpha_{ib,1} = 1 - \exp(-\alpha_{ib} \frac{d}{2}) \tag{3.21}$$

3.3.4 First Fresnel absorption.

The first Fresnel absorption at each point is included in the energy balance by multiplying the local beam intensity by the Fresnel absorption coefficient, α_{Fr} due to the local wall angle θ_w, as applied in (3.18). The beam intensity is already damped by the plasma plume(3.20), and by the first plasma absorption(3.21). The inclination of the beam to the wall results from the z-dependence of the beam intensity (3.14).

In practice, directly tabulated values of α_{Fr} are difficult to obtain, but a reasonable approximation for the incident wavelengths n the infrared by relating the absorptivity to he temperature-dependent value of the electrical resistivity according to the following equation taken from Infrared Radiation: A Handbook for Applications by Bramson, M.A. (Plenum, New York, 1968).

$$\alpha_{Fr} = 0.365\left(\frac{\gamma}{\lambda}\right)^{1/2} - 0.0667\left(\frac{\gamma}{\lambda}\right) + 0.006\left(\frac{\gamma}{\lambda}\right)^{3/2} \tag{3.22}$$

where γ is the resistivity and λ is the incident laser wave length.

3.3.5 Fresnel absorption during multiple reflections.

The reflected part of the intensity undergoes multiple reflections in the keyhole. Assuming the Fresnel absorption coefficient to be constant and equal to the value for normal incidence, the overall absorption can be estimated. This approximation is valid for multiple reflections due to the fact that the angle of incidence successively increases. The absorption coefficient α_{mr}, is given by

$$\alpha_{mr} = 1 - [\rho_{Fr}(\pi/2)]^{(\pi/(4\theta_w) - 1)} \tag{3.23}$$

where $\rho_{Fr}(\theta)$is the Fresnel reflection coefficient and θ_w is the mean wall angle.
These values are shown in the graph in the following figure 3.5. It can be seen that the absorption falls off rapidly with increase in angle due to the decreasing number of reflections.

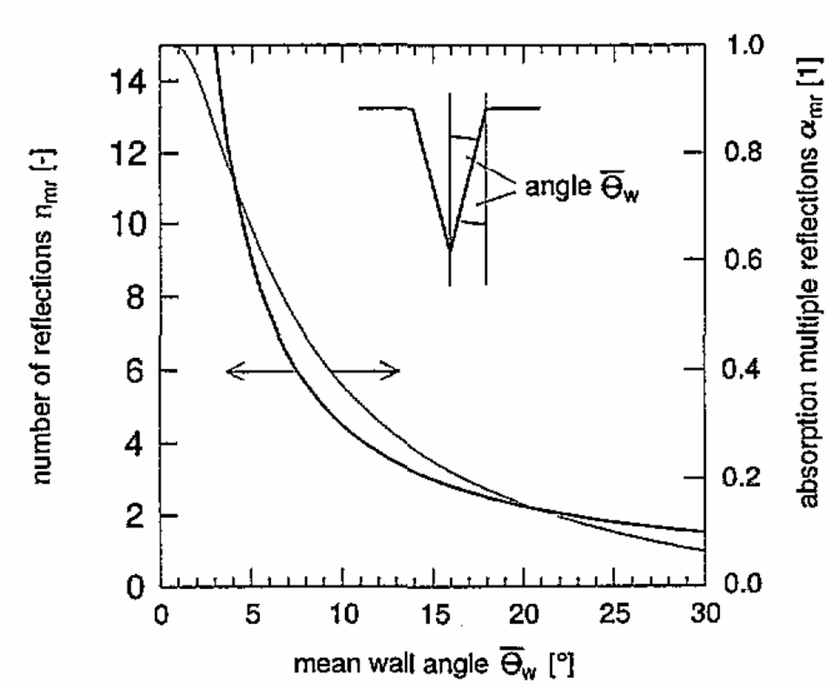

Figure 3. 5 Absorption coefficient of multiple reflections.

3.3.6 Plasma absorption during multiple reflections.

During each reflection the rays cross the plasma and are partially absorbed by it. This effect is modeled by using the value of intensity that is left after undergoing multiple reflection and then by defining the mean path of rays to be one and half times the depth for the case of a blind keyhole.

$$\alpha_{iB,mr} = 1 - \exp\left(-\alpha_{iB}\frac{3d}{2}\right) \tag{3.24}$$

3.3.7 Governing Equations.

The values used in the equation (3.19) resulting from the absorption sequence in figure 3.4 can be summarized as follows;

$$I_{a,Fr} = (1-\alpha_{pl})(1-\alpha_{iB,1})\alpha_{Fr} I(x,z) \tag{3.25}$$

$$I_{a,mr} = (1-\alpha_{pl})(1-\alpha_{iB,1})(1-\alpha_{Fr})\alpha_{mr} I(x,z) \tag{3.26}$$

$$I_{a,iB} = (1-\alpha_{pl})(\alpha_{iB} + \alpha_{iB,mr}(1-\alpha_{iB,1})(1-\alpha_{Fr})(1-\alpha_{mr}))I(x,z) \tag{3.27}$$

The sum of (3.25) - (3.27) is the incident intensity damped by the plume minus the remaining intensity I_r leaving the keyhole.

$$I_{a,Fr} + I_{a,mr} + I_{a,iB} = (1-\alpha_{pl}) I(x,z) - I_r \tag{3.28}$$

where
$$I_r = (1-\alpha_{pl})(1-\alpha_{iB,1})(1-\alpha_{Fr})(1-\alpha_{mr})(1-\alpha_{iB,mr}) I(x,z) \tag{3.29}$$

3.4 Kaplan's findings & Conclusions

Kaplan had used the model by applying it to find the effect of welding speed on the absorption behavior for a laser unit of 4kW power and 10 kW power. Furthermore, the calculated welding depth has been compared with the experimental values and the keyhole profile discussed.

3.4.1 Geometrical Observations

The resulting keyhole profile for 4 kW and 50 mm s-' is drawn in figure 3.6 and 3.7. Figure 3.6 shows that the keyhole and melt pool are both long and narrow as expected in deep penetration laser welding. In figure 3.7 the x axis has been magnified to see the geometrical behavior of the profile.

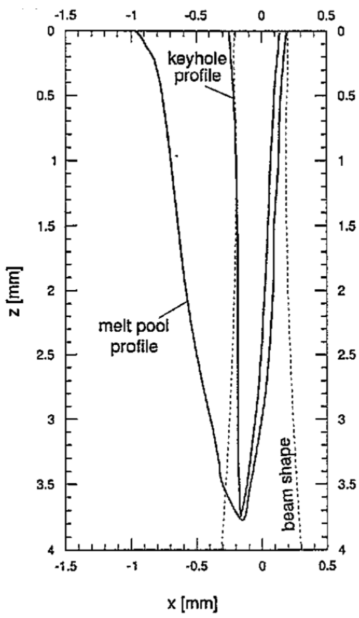

Figure 3. 6 Key Hole Profile for 4kW and 50mm/s Laser.

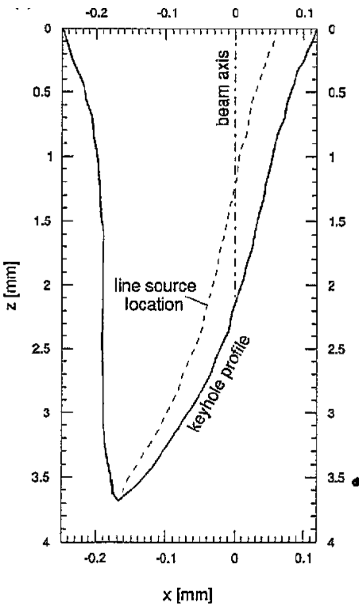

Figure 3. 7 Key Hole Profile magnified in x direction.

The beam axis is located at the middle of the front wall indicating that the major part of the beam hits the front part of the keyhole and regions of the beam with lower intensity are sufficient to hold the rear wall stable. This effect can be explained by the heat conduction which is much stronger at the front wall due to the convective effect of the welding speed.

The front wall is less steep than the rear wall so that it is able to intercept enough of the beam to balance the conduction losses.

The wall geometry is mainly defined by the first Fresnel absorption, whereas the other absorption mechanisms have an isotropic effect on both sides. The effect is similar to the initiation of an absorption front in laser cutting. The back wall is nearly balanced by the absorption due to multiple reflections and inverse Bremsstrahlung and needs only some further direct input from relatively low laser intensity. The curvature of the rear wall is slightly inclined backwards following the beam caustic surface.

3.4.2 Absorption Characteristics.

Near the keyhole wall absorption is lower than 50 m^{-1} and can be neglected. Adjacent to the wall, it increases steeply up to the maximum value, which is higher than 200m^{-1} for iron. In most of the keyhole the absorption reaches values in the range 50 - 200 m^{-1}, therefore, averaging leads to a mean absorption coefficient of about 100 m^{-1} for iron for each depth of the keyhole. The central zone of the keyhole has low absorption because the coefficient decreases at temperatures exceeding 12 000 K.

3.4.2.1 Plasma Plume Damping

The out flowing metal vapor leads to a flow field as drawn in figure 3.8 below. The absorbing core of the vapor flow has a mean plume height of 1.2 mm. For an absorption coefficient of $\alpha_{iB,mr} = 100\ m^{-1}$ the absorption losses of the plume are 8%. if all absorbed power in the plume is assumed to be removed by radiation and convection rather than being conducted to the work piece.

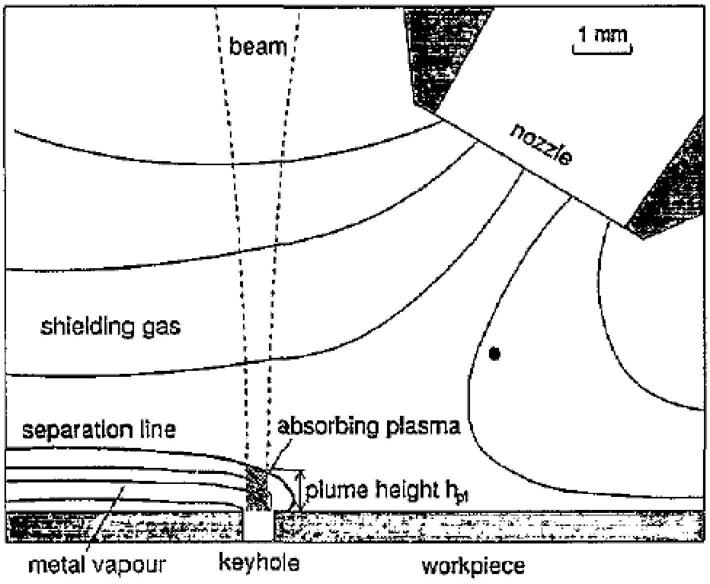

Figure 3. 8 Flow Field near the Keyhole.

3.4.2.2 Power on the work piece.

The fraction of the beam that hits the work piece outside the keyhole is plotted in figure 3.9 as a function of the welding speed.

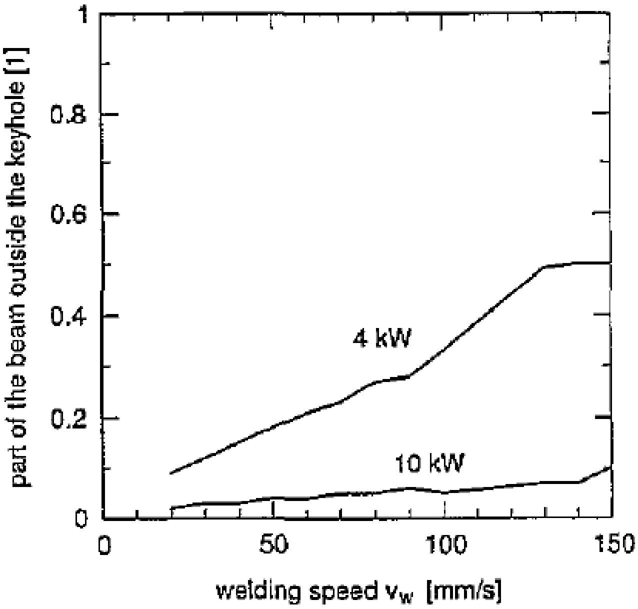

Figure 3.9 Power on the work piece vs. Welding speed.

The fraction increases with increasing speed due to the higher intensity necessary to initiate keyhole formation. For 10 kW the intensities in the beam are very high; thus, at all speeds only a small fraction of the beam does not take part in keyhole formation. In the case of 4 kW power the fraction increases considerably with rising welding speed. The starting point of the keyhole shifts towards the centre of the beam and for velocities higher than 120 mms^{-1} nearly half of the beam is wasted. Intensities very close to the maximum intensity on the beam axis are necessary to balance the convection losses involved at high welding speeds.

3.4.2.3 Absorptions within the keyhole.

The resulting overall absorption balance is shown in figure 3.10 for 4 kW laser power and in figure 3.11 for 10 kW.

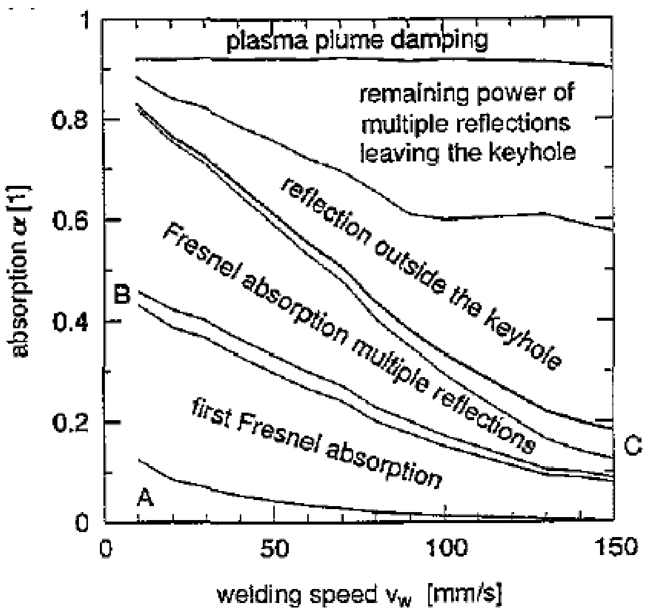

Figure 3.10 Power Absorption Balance for 4kW Laser

The strongest absorption mechanisms are direct Fresnel absorption and absorption by multiple reflections, whereas plasma absorption is negligible. The overall absorption decreases with increasing welding speed because the various mechanisms all decrease except absorption outside the keyhole, which is not very strong and has no effect on keyhole formation.

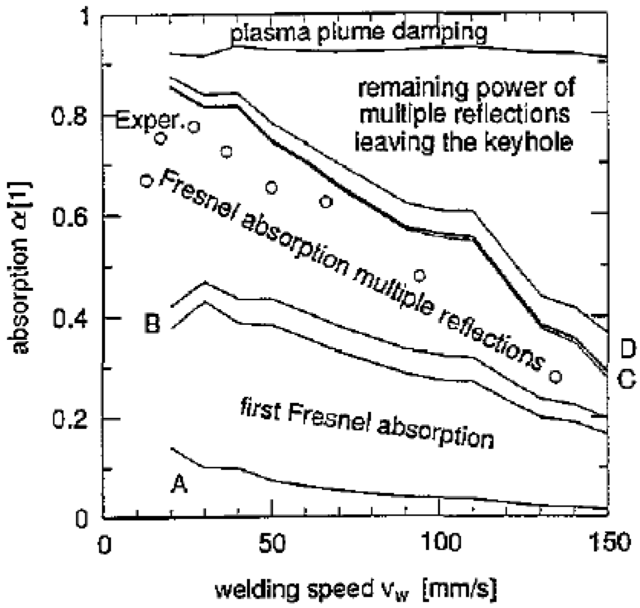

Figure 3.11 Power Absorption Balance for 10kW Laser

For 10 kW the behavior is similar except that the losses due to radiation hitting the work piece outside the keyhole are much smaller than for 4 kW.

3.4.3 Summary of Conclusions.

The main findings and conclusions of Kaplan can be summarized as follows.

(i) The heat losses at the up streaming front side of the keyhole are much larger than at the down streaming side, except for low speeds.

(ii) The only mechanism sufficient to balance this difference is direct Fresnel absorption when the rays first hit the keyhole wall.

(iii) Therefore the keyhole tends to a profile to transfer the greatest fraction of the directly absorbed beam to the front side, resulting in an inclination of the front wall similar to that in laser cutting.

(iv) A part of the beam hits the metal surface outside in front of the keyhole because intensities there are too low for keyhole ignition.

(v) The correlating power losses of (iv) become significant for low intensities and high welding speeds according to a threshold intensity for the spatial starting point of keyhole formation.

(vi) With decreasing penetration depth the keyhole opening angle increases reducing the average number of multiple reflections and the according absorption.

(vii) The overall absorption decreases with increasing welding speed.

(viii) Plasma absorption is much lower than Fresnel absorption

Chapter 4

Experiment

4.1 Material Selection & Parameters

Mild Steel was selected for the experiment as it is most commonly used material and thus all the data regarding the base metal are easily accessible. Table 4.1 lists the chemical composition of Mild steel as shown below.

Table 4.1 Chemical Composition

Chemical Composition (wt %)				
Fe	(0.08-0.13) C	(0.3-0.6) Mn	0.04 P max	0.05 S max

Table 4.2 below shows the mechanical properties of steel.

Table 4.2 Mechanical Properties

Mechanical Properties	
Hardness, Brinell	121
Hardness, Knoop	140
Hardness, Vickers	126
Tensile Strength, Ultimate, MPa	420
Tensile Strength, Yield, MPa	350
Elongation at Break, %	15
Modulus of Elasticity, GPa	200
Bulk Modulus, GPa	140
Poisson’s Ratio	0.25
Machinability, %	65
Shear Modulus, GPa	80

The thermal and mechanical properties are further illustrated in the graph below (fig 4.1)

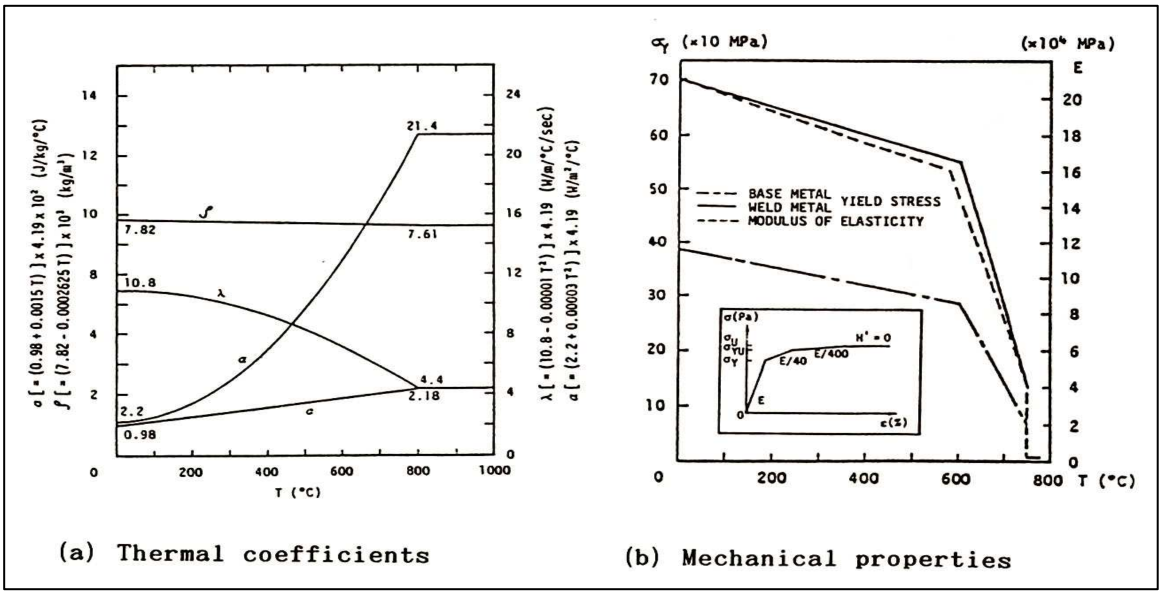

Figure 4.1 Thermal and mechanical Properties of Mild Steel

4.2 Fabrication of Work Piece.

Mild Steel of 6mm thickness was used to perform the experiment. The metal sheet was cleaned to avoid any surface impurities. Nd-YAG laser welding machine with a maximum power of 3 kW was used to make different keyholes using continuous mode. Three welding speeds(17mm/s, 25mm/s and 33mm/s) were used to obtain different keyhole profiles.

Two 200 X 100 X 6 mm dimension plates are joined by butt welding as shown in the simplified figure below (fig 4.2)

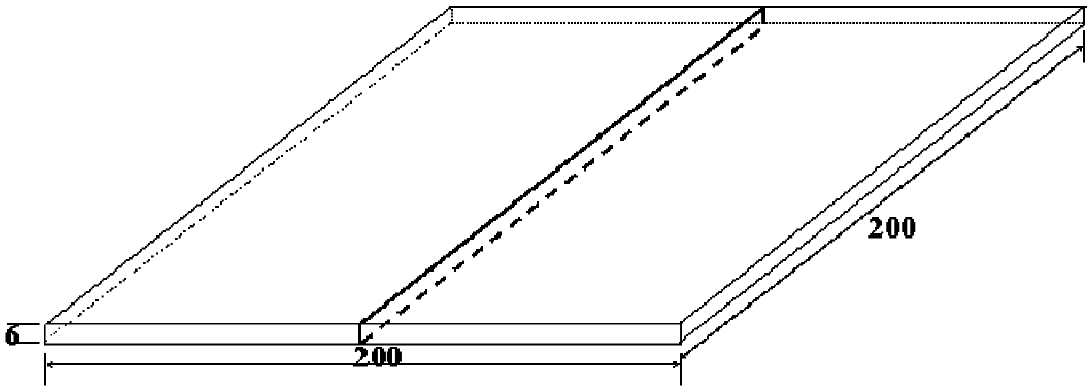

Figure 4.2 Specimen Dimension

The employed welding conditions are shown in the table 4.3 below. Figure 4.3 shows the picture of the laser welding machine used for the fabrication.

Table 4.3 Laser welding parameters

Wavelength, μm	1.064
focal length, mm	200
Beam Quality	1
Focal Radius, μm	100
Rayleigh length, μm	1600
Laser Power, kW	3
Welding Speed, mm/s	17, 25 and 33

Figure 4.3 Nd-YAG Laser Welding Machine

4.3 Experimental Results.

After the welding careful sectioning of the weld zone and keyhole was performed to determine the profile. This obtain profile was used for microscopic measurement of dimension. The resultant keyhole transverse and longitudinal sections are shown in the figures below. (figure 4.5~ 4.10)

The keyhole profile was measured form the sectioned weld zone using microscopic measurements. This shape was compared with the mathematical model for verification. Figure 4.4 shows the microscopic measurement devices in the lab.

Figure 4.4 Microscopic arrangements for dimension measurement

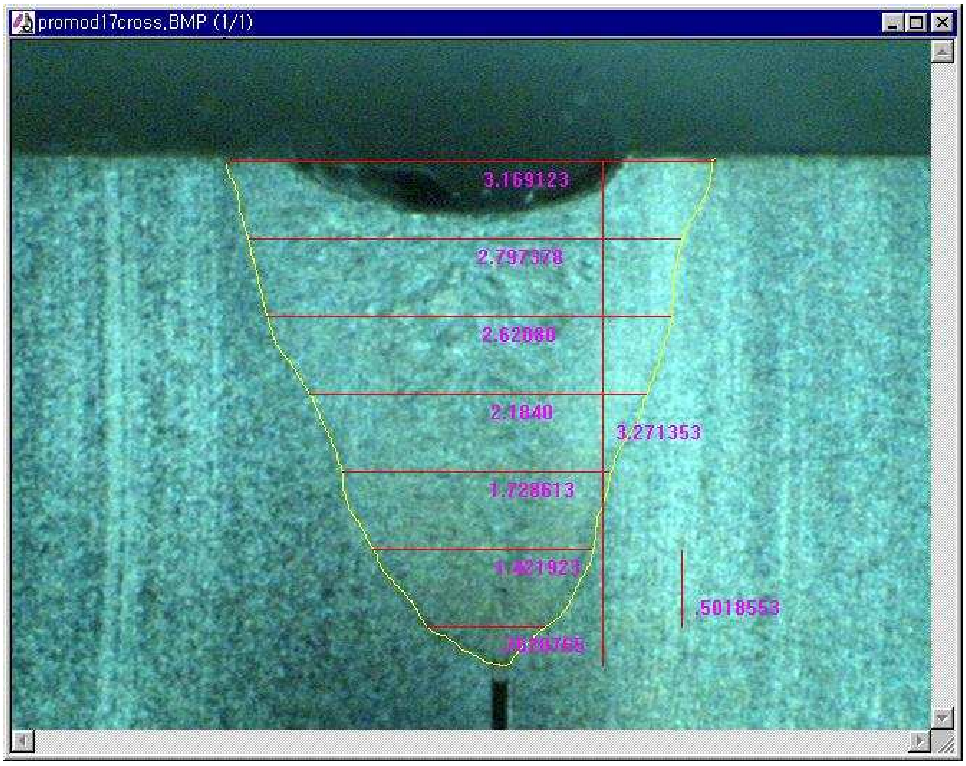

Figure 4.5 Section View and Measurement for 17mm/s speed

Figure 4.6 Longitudinal View and Measurement for 17mm/s speed

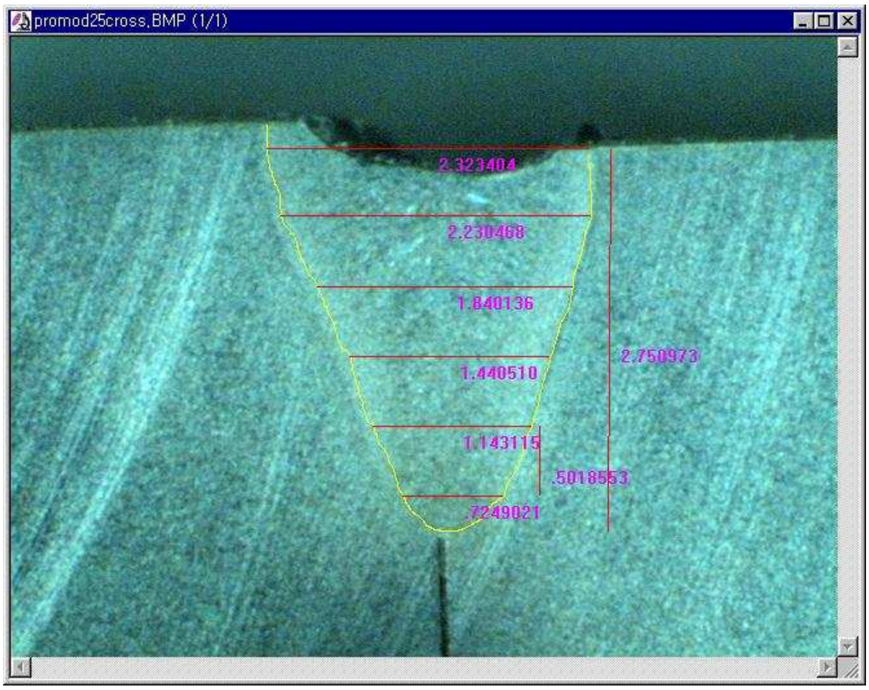

Figure 4.7 Section View and Measurement for 25mm/s speed

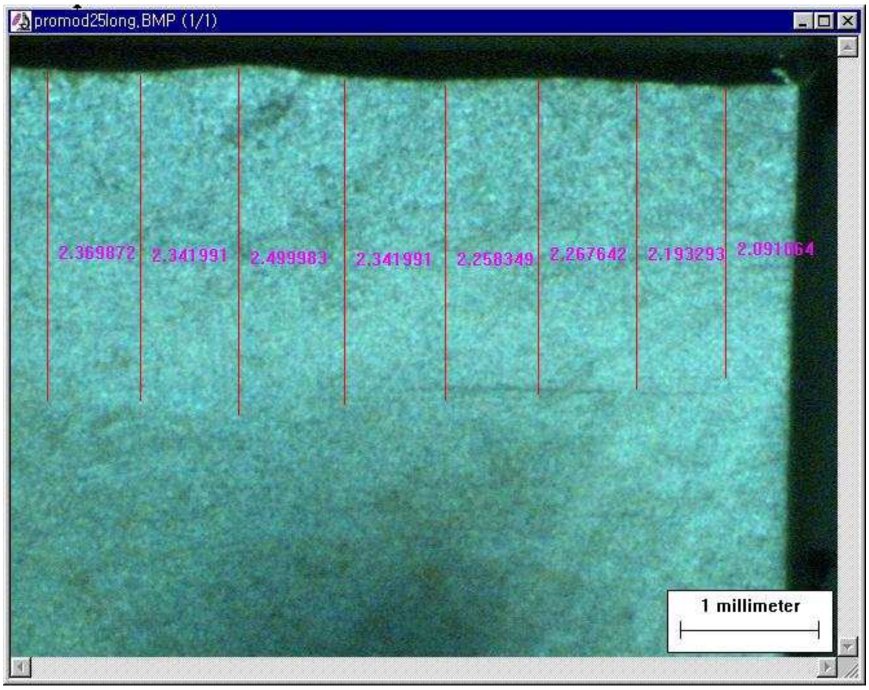

Figure 4.8 Longitudinal View and Measurement for 25mm/s speed

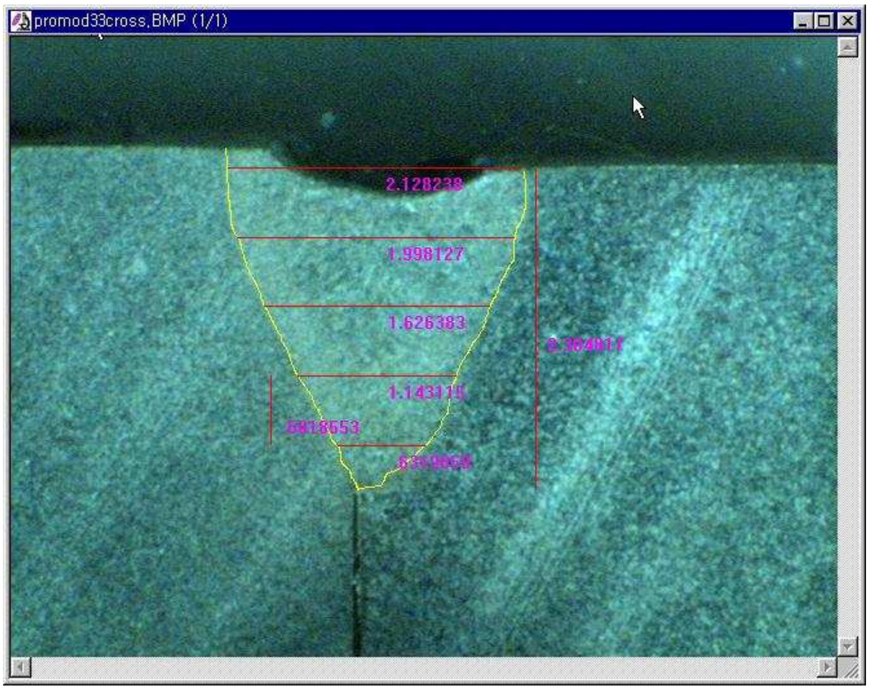

Figure 4.9 Section View and Measurement for 33mm/s speed

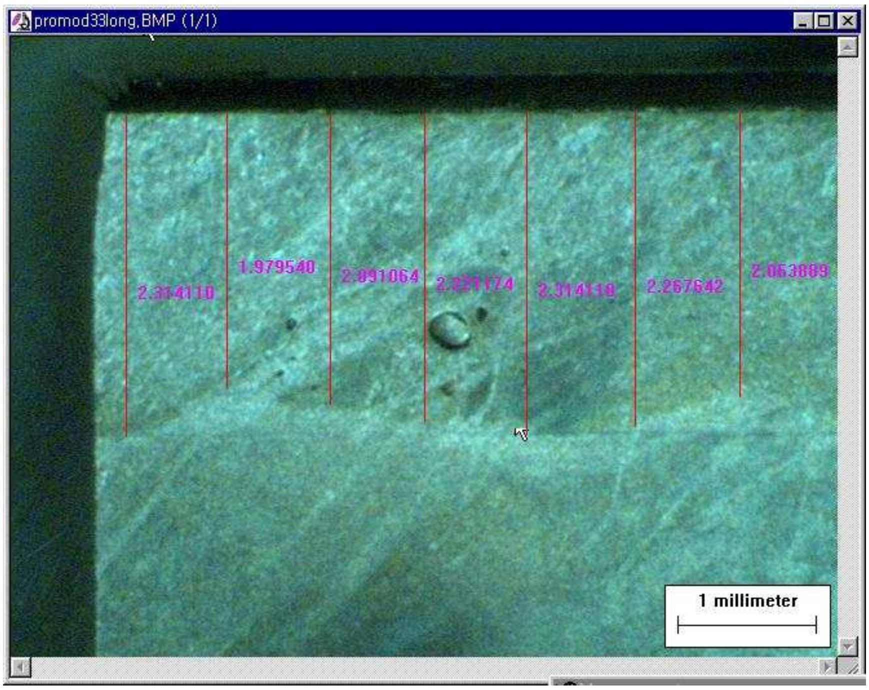

Figure 4.10 Longitudinal View and Measurement for 33mm/s speed

Chapter 5

Results and Discussions

5.1 Assumptions and Justifications.

The model uses a heat flux balance at the edge of the keyhole wall in order to estimate the depth and width of the vapor cavity. The following assumptions are made: first, that the keyhole wall temperature is equal to the boiling point of the material; second, that the heat transfer along directions perpendicular to the incident laser beam (parallel to the welding surface) is much faster than along directions parallel to the beam; and third, that the plasma in the keyhole has a constant absorption coefficient, independent of position. The first assumption is reasonable since the system is open to the atmosphere. The second also holds, since the keyhole is nearly vertical, and the keyhole wall temperature is assumed to be equal to the boiling point of the material, giving rise to primarily radial heat transfer away from the laser keyhole. The third assumption has little theoretical justification, but in practice, the energy loss due to absorption in the plasma is quite small for Nd:YAG laser welding, so the overall error in beam intensity due to this approximation is minor, and calculations are simplified considerably.

5.2 Keyhole calculations.

Keyhole calculations were done for 5 different speeds 13mm/s, 17mm/s, 25mm/s, 33mm/s and 41mm/s. Table 5.1 below shows the different constants used for the calculation for the keyhole shapes. A constant power 3kW is used for all the calculations.

In order to obtain a simplified calculation for the keyhole shape the following assumptions are made;

- Keyhole geometry Influenced only by Fresnal Absorption and further absorption mechanisms not considered for simplicity.
- A reasonable approximate formula for Fresnal Absorption Coefficient used and assumed to be constant.

Table 5.1 Constants used for the Keyhole Calculations

Material Constants							
1)	Tv	=	2073	Vapourisation Temperature of Mild Steel, K			
2)	Ta	=	298	Room Temperature, K			
3)	λ_{th}	=	26.9	Thermal Conductivity, W/·m·K	2.69E-02	W/mm K	at 1200K
4)	ρ	=	7500	Density of Mild Steel, kg/m^3	7.50E-06	kg/mm^3	at 1122K
5)	Cp	=	107.78	Specific Heat Capacity, J/kg K	1.08E+08	mm^2/s^2 K	at 1255 K
6)	κ	=	3.33E-05	Thermal Diffusivity, m^2/s	3.33E+01	mm^2/s	at 1066K
Laser Parameters							
1)	λ	=	1.064	Wavelength, µm	1.06E-03	mm	
2)	f	=	200	focal length, mm			
3)	D_b	=	25	Beam Diameter, mm			
4)	F	=	8	Focusing number, = focal length/beam diameter on optics			
5)	M^2	=	1	Beam Quality			
6)	r_{f0}	=	100	Focal Radius, µm	0.10	mm	
7)	Zr	=	1600	Rayleigh length, µm	1.60	mm	
8)	P_L	=	3	Laser Power,kW			
9)	I_0	=	190985932	Peak Intensity, kW/m^2	190.99	kW/mm^2	
10)	γ	=	1.20E-06	Electrical resistivity, Ω-m	1.20E-03	Ω-mm	
11)	α	=	0.32	Fresnal Absorbtion Coefficient			

Microsoft Office Excel is used for the calculation of the keyhole shape. A sample calculation sheet for a speed of 13mm/s is given in Table 5.2 below.

As the tool itself is not powerful enough to do iterations, it is unable to predict the actual shape of the keyhole especially near the surface of the plate. An assumption of 45 degree slope at a point 0.1mm below the surface is assume to get the initial point. However, the assumption does not vary the shape well below the surface and hence the maximum depth obtained is comparable with the experimental values as shown later in this section. Calculations are done for three angles 0, 90 and 180 to obtain profiles in both transverse and longitudinal direction.

Table 5.2 Calculation sheets for keyhole shape

Calculation Sheets

1) Vw= 13mm/s

Input the increment value, Δz = 0.16 mm

No	r (mm)	z (mm)	υ_∞ (mm/s)	Pe'(=$\upsilon_\infty/2\kappa$) (mm^{-1})	φ (deg)	r_f (mm)	q_v (W/mm^2)	I(r,z) W/mm^2	θ_∞ (deg)
1	0.18171	0.1	13	0.19532621	0	0.10019512	85.1744417	85.18399574	45.00
2	0.019228	0.263	13	0.19532621	0	0.10133689	444.924393	58307.04866	0.44
3	0.017988	0.425	13	0.19532621	0	0.10346771	469.572068	61491.42322	0.44
4	0.016747	0.588	13	0.19532621	0	0.10652824	497.62491	65905.30711	0.43
5	0.01552	0.750	13	0.19532621	0	0.11044123	529.45215	71542.97003	0.42
6	0.014318	0.913	13	0.19532621	0	0.11511978	565.556425	78401.09061	0.41
7	0.013146	1.075	13	0.19532621	0	0.12047473	606.648646	86478.5803	0.40
8	0.012006	1.238	13	0.19532621	0	0.12642016	653.753834	95776.13299	0.39
9	0.010896	1.400	13	0.19532621	0	0.13287682	708.375001	106295.6737	0.38
10	0.009813	1.563	13	0.19532621	0	0.1397739	772.769357	118039.8387	0.38
11	0.00875	1.725	13	0.19532621	0	0.14704943	850.451545	131011.5528	0.37
12	0.007695	1.888	13	0.19532621	0	0.15465001	947.189734	145213.7135	0.37
13	0.006635	2.050	13	0.19532621	0	0.16253005	1073.18823	160648.9567	0.38
14	0.005549	2.213	13	0.19532621	0	0.17065083	1248.57199	177319.4446	0.40
15	0.004405	2.375	13	0.19532621	0	0.17897958	1520.22072	195226.5582	0.45
16	0.00314	2.538	13	0.19532621	0	0.18748861	2033.60394	214370.1188	0.54
17	0.001598	2.700	13	0.19532621	0	0.19615444	3658.20517	234745.1741	0.89
18	-0.00093	2.863	13	0.19532621	0	0.20495718	#NUM!	256310.4421	#NUM!

The calculation as shown in the above table is repeated for angles of 90 and 180 degrees. From the equation it can be seen that the values for the 270 degrees are same as that of 90 degrees. Thus we obtain approximate keyhole profiles for each speed as follows (fig 5.1 ~ 5.5).

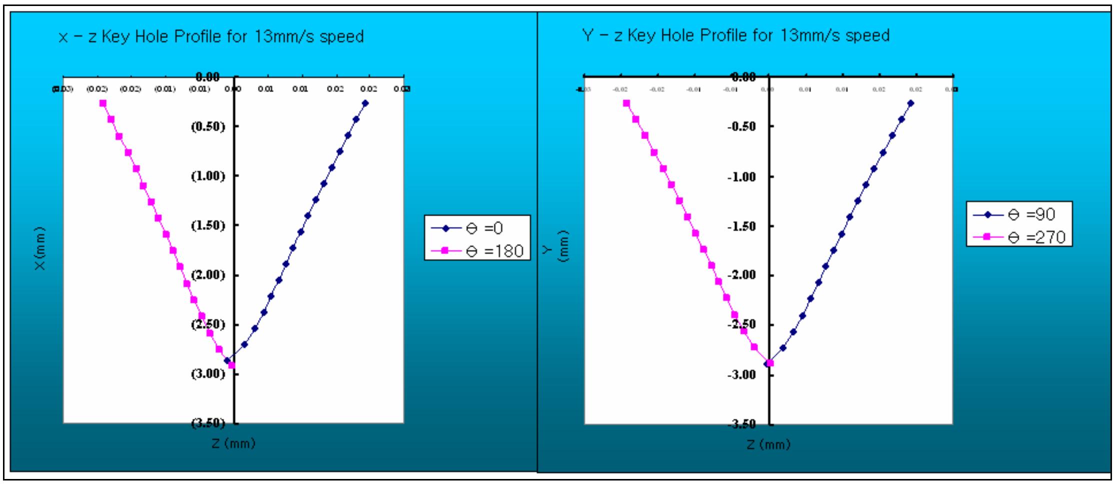

Figure 5. 1 Keyhole Profile for 13mm/s

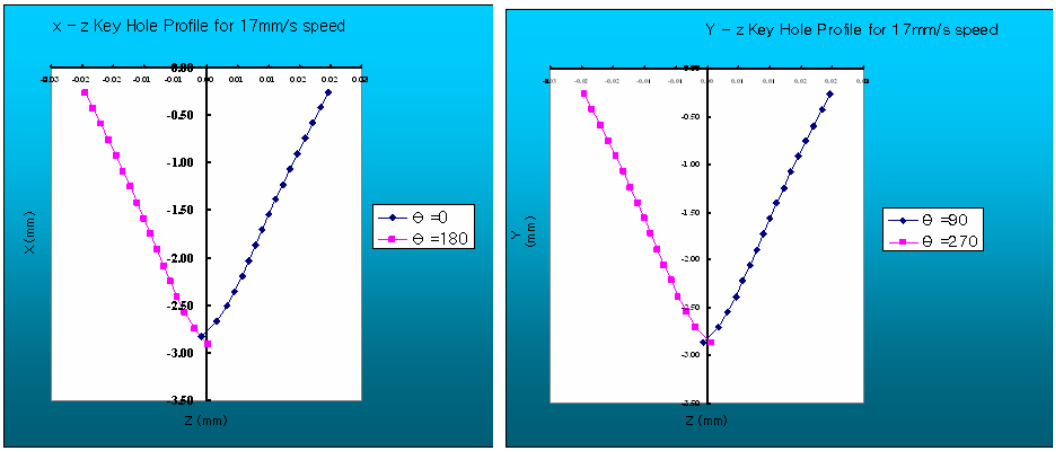

Figure 5. 2 Keyhole Profile for 17mm/s

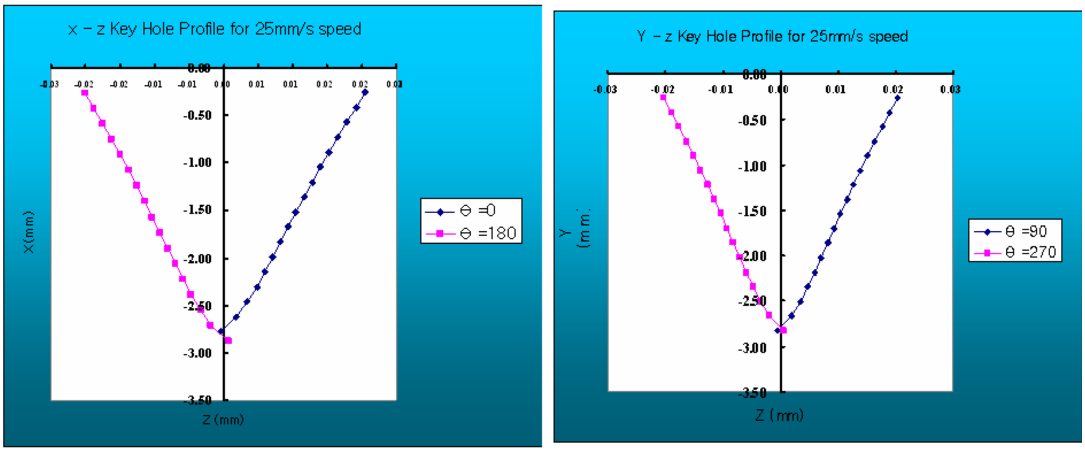

Figure 5. 3 Keyhole Profile for 25mm/s

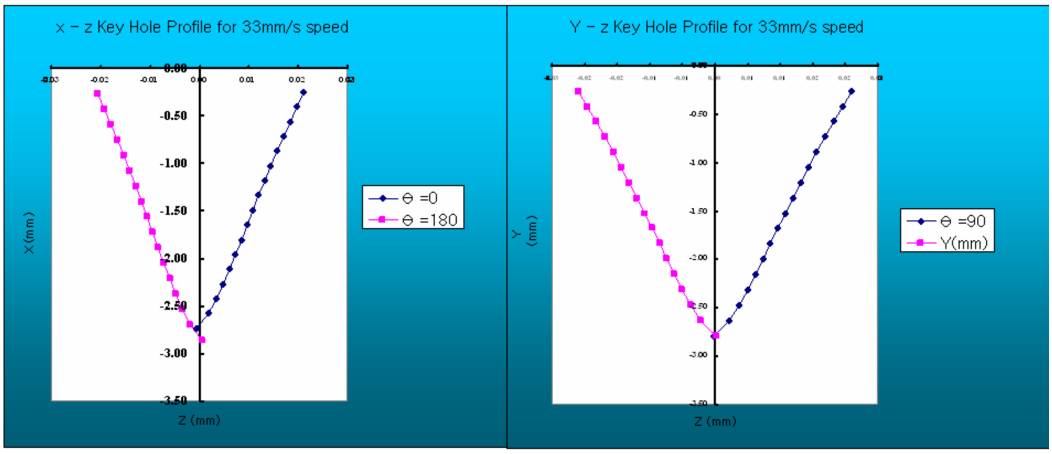

Figure 5. 4 Keyhole Profile for 33mm/s

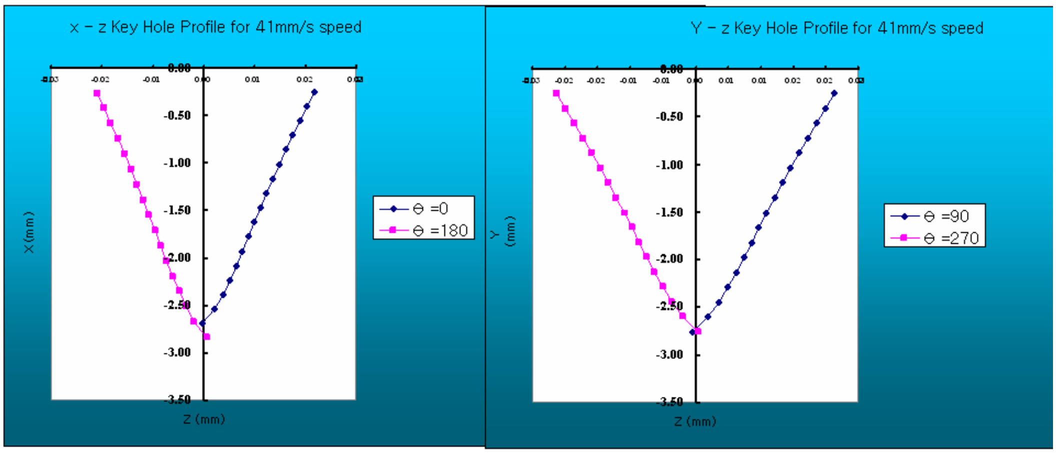

Figure 5. 5 Keyhole Profile for 41mm/s

All the graphs have been enlarged in the x-direction to get a clear idea of the keyhole profile. It can be seen that the depth decreases with increase in speed which is quite logical. Another observation is that the keyhole profile is not symmetric in the longitudinal section. The reason for this is the different effect of convective heat transfer at the front and rear wall due to the direction and speed of welding.

5.3 Experimental Verification.

As mentioned in the previous chapter, experiments were performed for three different speeds 17mm/s, 25mm/s and 33mm/s. The maximum depth obtained during the experiments were compared with the calculated values as shown in the following figure 5.6

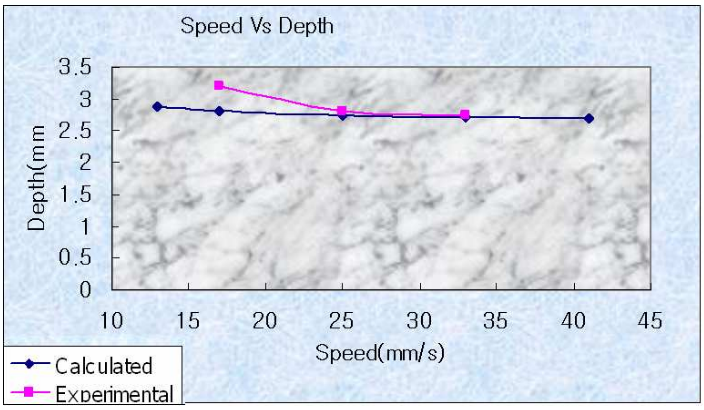

Figure 5. 6 Comparison of welding depth.

As expected, the calculated values are lesser than the experimental values. This is due to the fact that in the calculations, the presence of molten metal below the vapor cavity. It can also be seen that as the welding speed decreases the difference increases. This is because for low and decreasing speed, the losses due to evaporation or plume effect increases. With the decreasing welding depth the opening angle also increases thus reducing the average number of multiple reflections.

5.4 Numerical Verification.

The heat flow calculated is a function of the radius and the depth of the keyhole. This heat flow is input in the in-house heat analysis program to see the heat distribution within the keyhole. This heat distribution is further used to run the second module of the program to calculate the residual stresses within the base metal.

5.4.1 Heat Transfer Analysis.

As mentioned in the second chapter of this report, an in-house finite element program is used for the heat transfer analysis. The analysis is done only for one speed of 13mm/s as verification to the mathematical model and experimental result. Figure 5.6 below shows the heat distribution in the welded area.

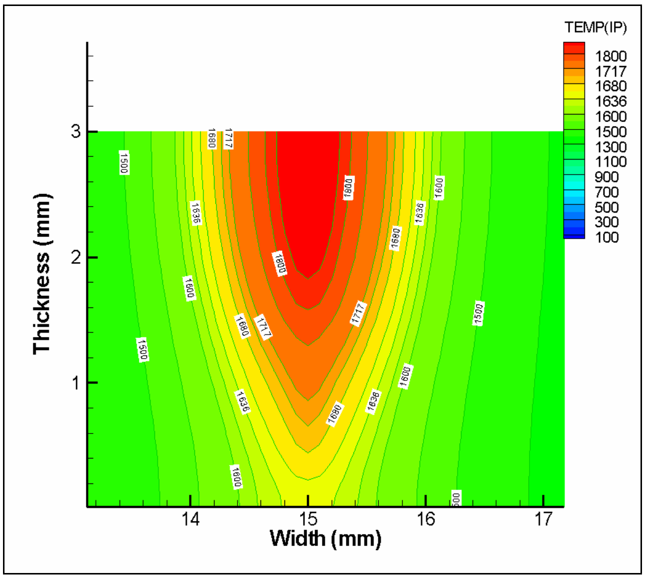

Figure 5. 7 Temperature Distributions for 13mm/s

On close examination, the melt zone can also be identified (where temp is around 2525K) and can be seen having similar shape to the experimental results. Deviations are expected as many of the properties like thermal conductivity, specific heat, density, and Fresnal absorption coefficient are all temperature dependent. In the calculations, however, all are taken as constants.

The figure5.8 below shows the thermal history of the welding for 13mm/s speed. From the graph the rate of cooling can be determined for each of the zones shown.

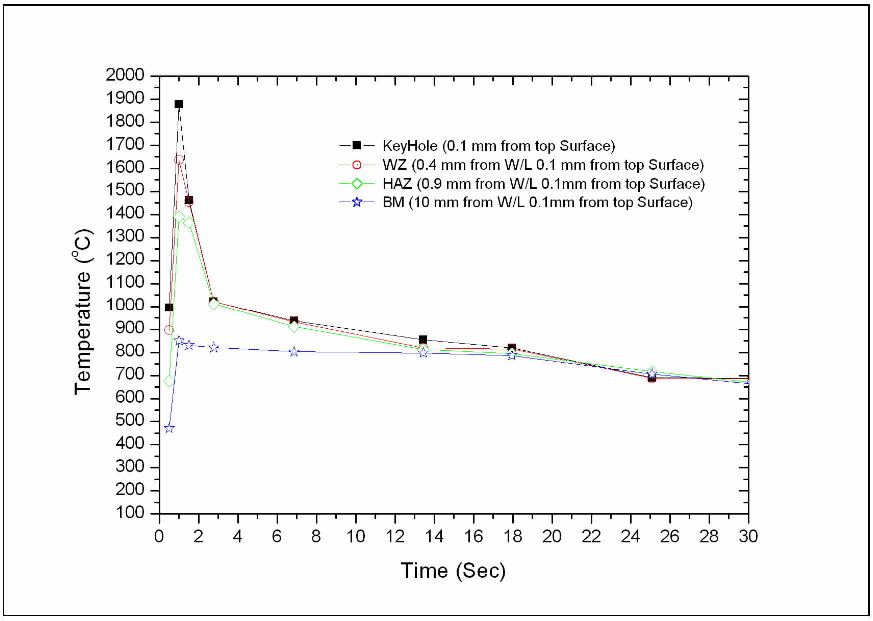

Figure 5. 8 Thermal history graphs for 13mm/s welding speed.

5.4.2 Residual Stress Determination.

From the output of the heat transfer analysis, the second module is run to calculate the residual stresses in the base metal. The following graph shows the residual stress distribution. From the graph it can be seen that the residual stresses accounts to about 21.3% of yield stress(figure 5.9).

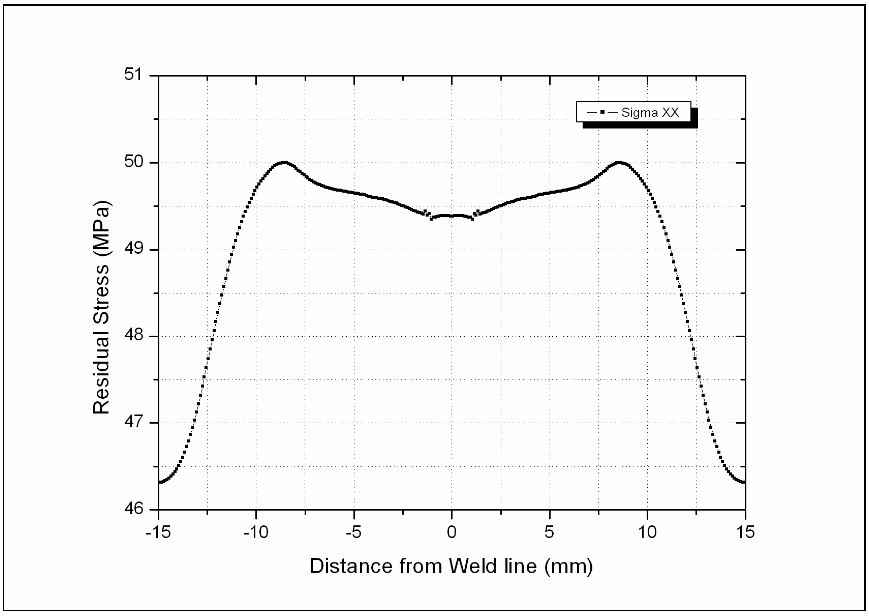

Figure 5. 9 Residual Stress Distribution.

5.5 Future Modifications.

The simplified keyhole calculations include only the effect of Fresnal absorption coefficients. Even though the results are reasonable, a further improvement is required which incorporates all the absorption mechanisms including the inverse Brensstrahlung absorption coefficient which is currently unavailable for the ND-YAG laser.

Another modification would be the introduction of coding and powerful iteration tools which can handle complex functions like the Bessel functions and thus can more accurately predict the keyhole shape especially towards the surface.

The mathematical model also needs to be further verified for a wide range of laser powers and speeds. It should be extended to different kinds of materials. The main constraint factors for this remains in limitation of the lab facility and high reflectivity of certain materials.

Chapter 6

Conclusions

The resulting keyhole profile shows that most of the beam hits the keyhole at the front wall whereas the rear wall of the keyhole is formed by low-intensity regions of the beam. The reason for this is the different effect of convective heat transfer at the front and rear walls due to the direction and speed of welding. The front wall tends to an angle sufficiently large to intercept enough of the beam to balance the heat losses. This behavior has similarities to the wall formation in laser cutting. The back wall is much steeper and its lower part can also diverge. Only the first, direct Fresnel absorption determines the wall formation; the other absorption mechanisms have nearly isotropic effects at the front and rear walls and have no strong angle dependence.

The determination of the plasma absorption coefficient in the keyhole for the Nd-YAG laser welding is practically difficult and it has been ignored in this report.

The overall absorption decreases with increasing welding speed. There are three reasons for this effect. The direct Fresnel absorption decreases, the number of multiple reflections and therefore the Fresnel absorption due to multiple reflections decreases and the part of the beam hitting the surface outside the keyhole increases with rising welding speed and rising power, resulting in decreasing depth and increasing wall angle. Lower beam intensities lead to higher fractions of the beam that cannot start keyhole formation and consequently hit the surface outside the keyhole.

Finally it can be concluded that Kaplan’s model can be used as a reasonable approximation for Nd-YAG Laser welding for low speed as well.

Reference

[1]. Andrew JG and Atthey DR 1976 J.Phys.D:Appl.Phys.9 2181-94

[2]. Beck M Berger P, Dausinger F and Hugel H 1991 Aspects of keyhole/melt interaction in high speed laser welding Eight Int.Symp.on Gas Flow and Chemical Lasers (GSL, 10-14 September 1990,Madrid) ed J M Orza and C Domingo (Bellingham, WA: SPIE) pp 769-74

[3]. Beck M Berger P and Hugel H 1992 Modelling of keyhole/melt interaction in laser deep penetration welding ECLAT'92, Laser Treatment of Materials ed B L Mordike (Oberusel: DGM) pp 693-8

[4]. Born M and Wolf E 1980 Principles of Optics (Oxford: Pergamon)

[5]. Bronstein I N and Semendjajew K A 1985 Taschenbuch der Mathematik 22nde edn (Leipzig: Teubner)

[6]. Del Bello U, Rivela C, Cantello M and Penasa M1991 Energy balance in high power CO2 laser welding SPIE Proc. On Industrial and Scientific Uses of High-Power Lasers 1502 104-16

[7]. Dowden J, Postacioglu N, Davis M and Kapadia P 1987 J. Phys. D: Appl. Phys. 20 36-44

[8]. Hugel H 1992 Strahlwerkzeug Laser (Stuttgart: Teubner)

[9]. Hughes T P 1975 Plasmas and Laser Light (London: Adam Hilger)

[10]. Kaplan A 1992 Characterization of laser –induced plasma (Proc.10^{th} Congress of LASER'91 ed W Waidelich (Berlin: Springer) pp459-63

[11]. Kaplan A 1994 Dissertation TU Wien

[12]. Kar A, Rockstroh T and Mazumdar J 1992 J. Appl. Phys.71 2560-69

[13]. Klemens P G 1976 J. Appl.Phys. 47 2165-74

[14]. Knight C J 1979 AIAA J> 17 519-23

[15]. Lancaster J F 1986 The Physics of Welding (Oxford: Pergamon)

[16]. Rosenthal D 1946 Trans. ASME 48 848-66

[17]. Schuocker D 1992 Industrial Laser Annual Handbook ed D Belforte, M Levitt (Berlin: Springer) pp 67-73---1993 Review of mathematical models of high power laser material processing (in the framework of the EU-194 modelling group, printed at the Forschunginstitut flir Hochleistungsstrahltechnik der TU Wien) Laser Eng. To be published

[18]. Steen W M, Dowden J, Davis M and Kapadia P1988 J. Phys. D: Apply. Phys. 21

1255-60
[19]. Swift-Hook D T and Gick A E F 1973 Welding J. 52 492-9
[20]. Wei P S, Wu T H and Chow Y T 1990 J. Heat. Transfer 112 163-8
[21]. Palmer, T.A., B.C.Wood, J.W. Elmer,C. Westrich, et al., Characterization of Stainless Steel and Refractory Metal Welds Made Using a Diode-Pumped, Continuous Wave Nd:YAG Laser(UCRL_ID_146005).
[22]. Zhao, H. and T.DebRoy, A Computer Program for the Calculation of Keyhole Geometry and Temperature Field during High Energy Density Beam Welding(Unpublished research,2002).
[23]. Ready, J.F.,ed., Laser Institute of America Handbook of Laser Materials Processing. (Laser Institute of America and Mongolia Publishing, Inc., 2001).
[24]. Bramson, M.A., Infrared Radiation: A Handbook for Applications (Plenum, New York, 1968).
[25]. DebRoy, T. and S.A.David, Rev. Mod. Phys., 1995, 67(1), 85-112.
[26]. ZelDovich, Y.B., and Y.P. Raizer, Physics of Shock Waves and High Temperature Hydrodynamic Phenomena (Academic, New York, 1966).
[27]. Collur, M.M., A. Paul, and T. DebRoy, Metall. Trans.B, 1987, 18 B, 733-740.
[28]. Sahoo, P., M.M. Collur, and T.DebRoy, Metall. Trans.B, 1988, 19B, 967-972.
[29]. Zhao, H., D.R. White, and T. DebRoy, Inter.Mater. Rev., 1999, 44(6), 238-266.
[30]. Zhao, H. and T. DebRoy, Metall. Trans. B, 2001, 32B (1), 163-172.
[31]. Lide, D.R., ed., CRC Handbook of Chemistry and Physics, 81st ed. (CRC Press, FL, 2000).
[32]. Gerritsen, A.N., “Metallic Conductivity, Experimental Part” in: S. FI? Ge (ed.), Handbuch der Physik, Vol. 19 (Springer-Verlag, Berlin, 1956).
[33]. Kaye, G.W.C. and T.H. Laby, Tables of Physical and Chemical Constants (Longman, London, 1995).
[34]. Yaws, C.L., Handbook of Thermal Conductivity(Gulf Publishing, Houston, 1997).
[35]. Ho, C.Y. and Y.S. Touloukian, Purdue University Thermo physical Properties Research Center, TPRC Data Series, Thermo physical Properties of Matter: Thermal Conductivity(IFI, Plenum, New York, 1977).
[36]. Ho, C.Y., P.E. Liley, and R.W. Powell, National Bureau of Standards, National Standard Reference Data Series, No.16: Thermal Conductivity of Selected Materials, Pt.2(USGPO, Washington, D.C., 1968).
[37]. Mills, K.C., Recommended Values of Thermo physical Properties for Selected

Commercial Alloys(ASM, Materials Park, OH,2002).

[38]. Ho, C.Y. and Y.S. Touloukian, Purdue University Thermo physical Properties Research Center, TPRC Data Series, Thermo physical Properties of Matter: Specific Heat (IFI, Plenum, New York, 1977).

[39]. James, A. and M. Lord, VNR Index of Chemical and Physical Data (Van Nostrand Reinhold, New York,1992).

[40]. Chase, M.W., National Institute of Standard and Technology, NIST-JANAF Thermo chemical Tables, 4th ed., taken from J.Phys. Chem.Ref.Data, Monograph 9 (American Institute of Physics, NY, 1998).

[41]. Filing Code: SS-254,”AISI304&304L”(May 1971), Alloy Digest(ASM, Materials Park, OH, 2000).

[42]. Gmelins Handbuch der Anorganischen Chemie: Vanadium, 48, A2(Verlag Chemie, Weinheim, 1968), 454-6.

[43]. Gmelins Handbuch der Anorganischen Chemie: Tantal, 50, A2((Verlag Chemie, Weinheim, 1969), 386-7.

[44]. Grigoriev, I.S and E.Z. Meilikhov, Handbook of Physical Quantities(CRC Press, FL,1997).

[45]. Zinovev, V.E., Handbook of Thermo physical Properties of Metals at High Temperatures (Nova, New York, 1996).

[46]. Peckner, D. and I.M. Bernstein, Handbook of Stainless Steels(McGraw-Hill, New York,1977).

[47]. Meaden, G.T., Electrical Resistance of Metal (Plenum, New York, 1965).

[48]. Pitscheneder, W., Contributions to the Understanding and Optimization of Laser Surface Alloying, Doctoral Thesis, Department of Physical Metallurgy and Materials Testing, University of Leoben, Austria(2001),pp. 1-242.

[49]. Nonhof, C.J., Material Processing with Nd-Lasers(Electrochemical Publications Limited, Scotland,1988).

[50]. Filing Code: SS-327,”Armco Nitronic 40”(May 1976, revised August 1990),Alloy Digest(ASM, Materials Park, OH, 2000).

[51]. Barin, I. and O. Knacke, Thermo chemical Properties of Inorganic Substances (Verlag Stahleisen MBH, New York, 1973).

ACKNOWLEDGEMENTS

I would like to express my sincere gratitude to Prof. Han-Sur Bang for having provided me an opportunity to work under him. I thank him for his valuable guidance and suggestions during the course of this work.

This gives me a great opportunity to express my gratitude, to my parents Mr. Gopinathan and Mrs. Latha Gopinathan for being a constant source of strength and support. Special thanks go to my wife Sandya who always gave me strength and support.

I would like to extend my appreciation to PhD student Rajesh.S.R for his help that he has provided me. Mr. H. G. Park, my fellow lab mate also helped me with the experiments and lab settings. Also thanks to all my co-workers and friends for their help and support.